NUMERICAL AND EXPERIMENTAL INVESTIGATIONS ON THE USE OF MIST FLOW PROCESS IN REFRIGERATED DISPLAY CABINETS

J. MOUREH[1]*, G. LETANG[1], B. PALVADEAU[1], H. BOISSON[2]

[1] UMR Génie Industriel Alimentaire Cemagref-ENSIA-INAPG-INRA
Cemagref Antony Refrigerating Process Engineering Unit, Parc de Tourvoie,
BP 44 - 92163 Antony cedex, France
[2]IMFT Institut de Mécanique des Fluides de Toulouse
Av. du Professeur Camille Soula - 31400 Toulouse

*Corresponding author: jean.moureh@cemagref.fr

Abstract

Open Refrigerated Display Cabinets (RDCs) play an essential role in food preservation as they are considered as one of the weakest links of the cold chain. This study concerns the use of mist flow whereby fine water droplets are injected into the air curtain to improve the performance of RDCs. The deposition and evaporation of droplets on the surface of products partially compensate the radiative heat gained by the product by removing from it the amount of latent heat of the evaporated droplets. This mist-cooling process leads to a decrease in the surface temperature of the products.

In this paper, the velocity characteristics of the air curtain and the temperature levels on the product surface were investigated numerically and experimentally. The experiments were carried out on an actual display cabinet. Numerical modelling was performed using Fluent Computational Fluid Dynamics (CFD) software. Numerical predictions have been carried out using the Renormalization Group (RNG) k-ε turbulence model, and the boundary layer of the air curtain, was fully solved using the enhanced wall treatment procedure. Good agreement was seen between numerical and experimental data in single-phase flow. In two-phase flow, an Euler-Lagrange approach was adopted to predict the transport of droplets by the air curtain and their spatial distribution on the product surface of the RDC. An original UDF (User-Defined Function) was performed and built in the CFD numerical model in order to compute the deposited droplets while taking into account the evaporative flux of droplets on the product surface.

The two-phase flow model was used to provide a good insight into the process and to analyse the performance of the mist cooling process in terms of surface temperature decrease and the homogeneity of droplet deposition on the product surface of the RDC as a function of inlet droplet injection configurations.

Keywords: *air curtain, refrigerated display cabinet, computational fluid dynamics (CFD), heat transfer, mist flow, airflow.*

1. **Introduction**

In order to ensure product quality, the required temperature must be maintained throughout the cold chain from production to consumption. In supermarkets and grocery stores, open-type refrigerated display cabinets (RDCs) are used extensively to merchandise perishable food at suitable temperatures.

A RDC consists of a limited container, insulating heat shell and a small refrigerating unit. The refrigerating system controls product storage temperatures by removing all of the heat gain components of the display case. RDCs operate by circulating cold air around the displayed products. Two or more fans circulate the air through an evaporator heat exchanger from the inlet to the outlet section. As a consequence, an air curtain which is a cold turbulent wall jet forms a non-physical barrier between the refrigerated load volume and the warm ambient air.

The advantage of the air curtains on RDCs is to allow consumers free access to food inside the cabinet [1], while at the same time preserving it at a suitable temperature. At the same time, air curtains also provide environmental separation by preventing the infiltration of pollutants, dust, dirt and insects. The main disadvantage of the air curtain compared with a glass-door cabinet is that it increases the radiative heat gained by the products. In addition, rather complicated mechanisms of flow, heat and mass transfer occur in the mixing zone between the air curtain and the ambience. The entrainment of warm ambient air causes the air curtain to become warmer between the inlet and outlet sections. Consequently, higher temperatures can be observed far downstream from the inlet jet, in the outlet area, due to the cumulative effect of the decaying of the refrigerated convective transfer of the air curtain and its warming.

RDCs are designed to keep food products at a specified temperature. The temperatures of the products displayed are maintained by the action of a refrigerated air curtain which should remove convectively, on the exposed product surface, the radiative heat exchanged by walls, lights and surroundings.

Many authors [2-9] have shown CFD modelling to be a promising and valuable tool to improve airflow efficiency in terms of energy savings and maintenance of the required temperatures. It can also be used to rapidly provide design options [3]. Stribling et al. [8] combined computational fluid dynamics and experimental results to predict airflow characteristics in a RDC. In a parametric study, Navaz et al. [7] used CFD to identify the significant parameters affecting the amount of entrained warm air in anRDC which is calculated as a function of the Reynolds number based on the jet width and velocity, and inlet turbulence intensity. Cortella [3] used the large eddy simulation turbulence model to predict the airflow pattern and food temperature on a vertical and a horizontal cabinet. In the latter case, the numerical results show that the temperature of the packages in the upper layer of the load is strongly dependent on their position, the warmest package being located close to the return air duct. This result was also observed by Bobbo et al. [10] who used a two-dimensional turbulence finite element method to simulate the temperature distribution within products. All of these studies have shown that the numerical and experimental results are in quite good agreement.

However, though improvements have been made on the technological content and airflow design of RDCs over the decades, it is hard to maintain correct storage temperatures in such refrigerators [11-12]. The performance of RDCs is affected by many factors, which include the dimensions of the air supply and return grilles, the width and the length of the air jets, the velocity and temperature of the air jets and the temperature, humidity and the air flow velocity of the ambient environment [1]. Various factors intrinsic as well as extrinsic to a cabinet can affect the distribution of refrigerated air along its length. As a consequence, RDCs can show very high temperature differences and it is often suggested that they are one of the weakest links in the chilled chain [3, 6, 11-16]. The presence of warmed products in the top layers caused by radiant heating or draughts of warm air entering cabinets has been reported by recent researchers [3, 12-13].

Regarding the difficulties encountered in keeping food at the required temperature in RDCs, the primary purpose of this project is to study the use of mist flow where fine water droplets are injected

into the air curtain to improve its refrigerated effect. The droplets carried by the air curtain are partially attached and evaporated on the warm surface of the products. Thus, the latent heat of the evaporated droplets makes it possible to absorb part of the radiative heat. This mist-cooling process leads to a decrease in the surface temperature of products and allows better compliance with European standards concerning safety considerations. Another important factor enhancing heat transfer by using mist flow is due to the fact that water droplets have higher specific heat capacity (*Cp*) than air. However, since the sensible heat of the water vapour is negligibly small compared with the sensible heat of the air or the latent heat of the water vapour in general, the specific heat capacity of saturated mist flow could be expressed as:

$$Cp_{\ mist\ \ flow} = \frac{d\hat{H}_{\ saturated\ \ humid\ \ air}}{dT} = Cp_{\ air} + Lv\ \frac{d\omega_{sat}}{dT} = Cp_{\ a}\left[1 + \frac{Lv}{Cp_{\ a}}\frac{d\omega_{sat}}{dT}\right] = Cp_{\ a}(\approx 2) \quad (1)$$

Where *Lv* and Cp_{air} are latent heat of water vaporization (2508 KJ/kg), the specific heat of dry air (1006J/kg.K) respectively, $\frac{d\omega_{sat}}{dT}$ is assumed to be a constant holding an average value of $0.4.10^{-03}$ (Kg water/Kg dry air . K) in the temperature range of 0-10°C [17]. Under these conditions, $Cp_{\ mist\ \ flow}$ is twice as high as Cp_a.

The mist flow cooling process is used in different domains such as heat exchangers, advanced turbine systems, fire safety, metallurgy and aeronautics. However, very few studies on the use of mist flow in refrigerating equipment have been reported. Brown et al. [18] used an ultrasonic humidification system to reduce water and weight loss in fruit and vegetables displayed in RDCs. The findings showed that humidification also reduced the rate of deterioration in the appearance of the produce on display. It can influence display life by reducing dehydration and perceived deterioration of quality. In addition, no adverse effects on the microbial quality of samples of produce were found. Allais and Alvarez [19] used the mist flow process to increase the heat transfer coefficient and to reduce water loss by the product during cooling. The study was performed in a packed bed of spheres simulating foodstuffs cooled by a two-phase flow of air and fine (8 μm) water droplets. The authors indicate that heat transfer was enhanced, compared with that obtained in single-phase flow: the maximum value rose to 2.8 under the experimental conditions. A marked heterogeneity of heat transfer was demonstrated and correlated to the local droplet deposition.

A general literature review [18-23] of jet impingement heat transfer in mist/air flow showed significant local cooling enhancement near the impact zone of the target surfaces or obstacles and very little effect elsewhere. This /strong heterogeneity aspect demonstrated the principal limitation of this process, since turbulent two-phase flows are difficult to control and resulted in non-uniform overcooling over the target surfaces [23]. Very little work has been done on local deposition or the heterogeneity of depositions, especially under the particular operating conditions generally encountered in refrigerated equipment. This means a highly transitional flow with strong near-wall interactions effects operating in conjunction with low air velocity, low heat flux, low surface temperature of the product (<15°C), and water supply regulated to avoid excess water on the product surface. This is important, because for some unwrapped food products, excess water can accelerate microbiological and biochemical changes responsible for food decay. Thus, the concept of RDC using the mist cooling process constitutes a very challenging task in experimental and numerical investigations. According to the uneven thermal heterogeneity within the RDC, there is a need to develop stochastic approaches to compute the trajectories of droplets and quantitative studies based on the coupling of the local droplet deposition and the local heat transfer on the product surface. These parameters are strongly influenced by air velocity, turbulence, and also inlet droplet injection configurations and the flow of water.

The objective of this study was to numerically and experimentally investigate the use of mist flow in a horizontal RDC in order to improve the air curtain efficiency. Special attention was paid to improvement of the homogeneity of droplet deposition along the product surface in accordance with

airflow, thermal behaviour and the actual design of the air curtain as generally encountered in RDCs. A better understanding of airflow and heat transfer mechanisms is clearly required in single phase-flow before applying mist flow. We present here CFD analysis of RDCs with and without mist injection and a comparison with experimental data obtained on an a full-scale display cabinet. Numerical predictions have been carried out using the Renormalization Group (RNG) k-ε turbulence model. In the air curtain, the boundary layer developed on the surface of products was fully solved using the enhanced wall treatment procedure. The adoption of such a procedure was preferable to the classical logarithmic laws governing the wall since it provides the most accurate predictions of surface temperature.

In two-phase flow, the model focuses on the transport of droplets by the air curtain and their spatial distribution on the product surface of the RDC as a function of inlet droplet injection configurations. To account for the influence of turbulent air fluctuations on droplets, the stochastic tracking Discrete Random walk model is used, which includes the effect of instantaneous turbulent velocity fluctuations on the particle trajectories. These approaches were successfully used to investigate the transport, dispersion and deposition of inert contaminant particles near walls or obstacles in indoor airflows operating at low velocities and turbulence [24-éè]. In this study, an original UDF (User Defined Function) was performed and built in the CFD numerical model in order to compute the deposited droplets while taking into account the evaporative flux of droplets at the product surface, evaporation being the main mechanism of heat transfer enhancement. The use of this UDF makes it possible to optimise the process in terms of water mass flow rate and inlet injection configuration in order to decrease the higher temperatures at the product surface while avoiding excess water in lower temperatures areas. The results obtained show that numerical simulation can be used in a predictive manner to optimise the use of mist cooling process in a RDC configuration.

2. EXPERIMENTAL DEVICE

The experimental measurements were performed on an actual RDC. The configuration investigated was designed for assisted sales and generally used for refrigerated cheese and meat products. The cabinet was considered as being full of products displayed on two horizontal surfaces separated by a step as shown in Figure 1. This step makes it possible to take into consideration the difference between the inlet and outlet levels.

The products were replaced by insulated medium. This avoids heat transfer by conduction through the products and makes it possible to obtain higher product surface temperature values.

Below the loading platform, two fans blow the air through an evaporator where it is cooled down. The cold air is blown into the cabinet through a perforated plate with 2-mm diameter holes. The inlet section is located 10 cm above the products with an inclination of 10° towards the products. Due to the Coanda effect, the issuing inlet jet should adhere to the product surface where it develops as a wall jet until the outlet section. Airflow and thermal measurements are performed on the mid-plane of RDC which represents the vertical plane on the centre line along the face of the cabinet. This prevents interactions with the cabinet boundaries.

Velocity was measured with a constant temperature hot-film transducer anemometer (Model 8455; TSI, Inc., USA). The probe could be used to measure the time-averaged velocities, but did not give any information on flow turbulence due to the considerably long response time (2 s). The operating range (0.125–1 m/s) covered the range of velocities encountered within the air curtain. In the factory calibration, the sensor was used with the main direction perpendicular to the sensor stem (accuracy ~3% of reading ~ 1% of full range).

A black painted thermal sensor is also used to measure locally the surface temperature along the cabinet. The black paint served to increase the emissivity of the sensor and thus to increase the

proportion of absorbed heat flux emitted by the external walls. This sensor is set precisely on the top plane representing the food surface in order to avoid a flow disturbance.
The temperatures of the air in the test room and in the air curtain were measured using a T-type thermocouple (previously calibrated, precision ± 0.2°C). All the measuring instruments are connected to a data logger (FLUKE HELIOS I). The experiments were performed in a room with a control of ambient conditions (T_a = *25* ± 0.2°C***;*** Hr_a = 60% and surrounding velocity V_a < 0.2 m/s).

The heat flux density was estimated through direct measurement of the radiative heat flux on the heated plate surface. Measurements were carried out with Captec radiant flux sensor. This sensor measures 40 x 40-mm wide and 3-mm thick, and has an integrated type-T thermocouple and therefore it allows temperature (*Tc*) and radiative heat flux (ϕ_r) to be measured independently. The external surface of the sensor was composed by alternating strips of lower and higher emissivities. This makes it possible to obtain a differential signal proportional to the radiative net heat density gauged at about 5.10^{-6} Volt/(W.m^{-2}) with a response time of about 100 ms. The relative uncertainty of the measurement remains lower than 5% for the range of heat flux variation in our experiment. For this sensor, the net radiative heat can be expressed as:

$$(\phi_r)_{net} = U / S \tag{2}$$

Where S and U represents respectively the sensitivity and the output voltage.
The incident heat flux radiation can be written:

$$(\phi_r)_i = (\phi_r)_{net} + \sigma T_c^4 \tag{3}$$

The mist generator was an ultrasonic humidifier. The water mass flow rate could be adjusted between 1.1 and 1.7 10^{-04} Kg.s^{-1} by modifying the electrical supply to piezoelectric elements. The Sauter mean droplet diameter was 4 μm.

3. Governing equations and numerical procedure

The description of temperature and airflow development was based on the conservative law of mass, motion and energy. Natural convection was considered by using the Boussinesq approximation in which density was treated as a constant value in all solved equations except for the buoyancy term in the momentum equations which was treated as: $(\rho_0-\rho)g=\rho_0\beta(T-T_0)g$, where ρ_0 and T_a are the reference density and temperature respectively, and β is the thermal expansion coefficient. The time-averaged solved equations for steady, incompressible, buoyant turbulent flows can be expressed as follows:

Mass conservation:
$$\frac{\partial \overline{U}_j}{\partial x_j} = 0 \tag{4}$$

Momentum conservation:

$$\frac{\partial \overline{U}_j \overline{U}_i}{\partial x_j} = -\frac{1}{\rho}\frac{\partial \overline{p}}{\partial x_i} + \frac{(\rho_0 - \rho)}{\rho_0} g\delta_{i3} + \frac{\partial}{\partial x_j}\left(\nu \frac{\partial \overline{U}_i}{\partial x_j} - \overline{u_i u_j} \right) + S_i^p \tag{5}$$

Energy conservation:
$$\frac{\partial \overline{U}_j T}{\partial x_j} = \frac{\partial}{\partial x_j}\left(\frac{\nu}{\mathrm{Pr}} \frac{\partial T}{\partial x_j} - \overline{u_j t} \right) + S_\phi \tag{6}$$

Where S_i^p , S_ϕ are user-defined source terms, and $\overline{u_i u_j}$ and $\overline{u_j t}$ are, respectively, the unknown Reynolds stresses and turbulent heat fluxes. Obtaining these quantities depends on the turbulence closure. Using the Boussinesq eddy viscosity concept, the Reynolds stresses can be described as follows:

$$-\overline{u_i u_j} = \nu_t \left(\frac{\partial U_i}{\partial x_j} + \frac{\partial U_j}{\partial x_i} \right) - \frac{2}{3} k \delta_{ij} \tag{7}$$

$$\overline{u_j t} = -\frac{\partial}{\partial x_j} \left(\frac{\nu_t}{\mathrm{Pr}_t} T \right) \tag{8}$$

3.1 Humidity equation

The basic assumption relating to the transport moisture modelling considers the air as a mixture of dry air–vapour. Moreover, no chemical interaction exists between these two species and their mixture is assumed as an ideal gas. The vapour mass fraction ω is defined as the ratio of the vapour mass contained in a given volume to the total mass of the mixture contained in the same volume. The conservation equation of ω is expressed as a convection-diffusion equation and added to the airflow model to take into account the distribution of water vapour mass fraction within the domain. This leads to:

$$\frac{\partial \overline{U}_j \omega}{\partial x_j} = \frac{\partial}{\partial x_j} \left(\left(D_m + \frac{\nu_t}{Sc_t} \right) \frac{\partial \omega}{\partial x_j} \right) \tag{9}$$

The value of moisture diffusivity (D_m) is 2.88 x 10^{-5} m^2 s^{-1} and the turbulent Schmidt (Sc_t) number value is 0.7. The steam fraction field was computed as a fluid component by taking into account the relative humidity of ambient air (Hr_a = 60%) and on the cabinet inlet section (Hr_0 = 100%).

3.2 Turbulence model

A significant property of turbulent jet flow is that momentum, heat and mass are transferred at rates much grater than those of the laminar flow with molecular transport processes by viscosity and diffusion. The numerical modelling of turbulent flows involves the modification of the governing equations for the case of the laminar flow using a time-averaging procedure known as Reynolds averaging [28].

3.2.1 The RNG *k-ε* turbulence model

Several considerations influence the choice of turbulence model. The most important criteria are related to the accuracy, the stability, the simplicity and the computational resources. A number of turbulence models were tested, including a standard *k-ε* turbulence model, RNG k-ε and Reynolds stress model. Preliminary studies showed the superiority of the RNG *k-ε* turbulence model in predicting the positions of reattachment points and velocity profiles related to the air curtain with the most accuracy. According to other workers, the RNG *k-ε* turbulence model has also been shown to better model separated flows and to perform well for studies of flow over complex configurations [27,29]. This turbulence model was therefore selected for the remaining studies.

The RNG-based *k-ε* turbulence model is derived from the instantaneous Navier-Stokes equations, using a mathematical technique called the RNG method [30]. In this approach, RNG techniques are used to develop a theory for the large scale in which the effects of the small scales are represented by modified transport coefficients. The RNG procedure employs a universal random force that drives the

small-scale velocity fluctuations and represents the effect of the large scales on the eddies in the inertial range. This force is chosen in such a way that the overall properties of the resulting flow field are the same as those in the flow driven by the mean strain. The RNG k-ε has a similar form to the standard k-ε model. The turbulent field is characterized in terms of two variables, the turbulent kinetic energy k, and the viscous dissipation rate of turbulent kinetic energy ε. Two transport equations for k and ε can be obtained from the Navier–Stokes equations by a sequence of algebraic manipulations. The analytical derivation results in a model with constants different from those in the standard k-ε model. The transport equations for k and ε provided by the RNG theory are:

$$\overline{U}_j \frac{\partial k}{\partial x_j} = \frac{\partial}{\partial x_j}\left[\alpha_k \nu_t \frac{\partial k}{\partial x_j}\right] + P_k - \varepsilon \tag{10}$$

$$\overline{U}_j \frac{\partial \varepsilon}{\partial x_j} = \frac{\partial}{\partial x_j}\left[\alpha_\varepsilon \nu_t \frac{\partial \varepsilon}{\partial x_j}\right] + C_{1\varepsilon} P_k \frac{\varepsilon}{k} - C_{2\varepsilon} \frac{\varepsilon^2}{k} - R_\varepsilon \tag{11}$$

P_k represents the shear production term:

$$P_k = \nu_t \left[\frac{\partial U_i}{\partial x_j} + \frac{\partial U_j}{\partial x_i}\right] \frac{\partial U_i}{\partial x_j} = \nu_t S^2 \tag{12}$$

Where S represents the modulus of the mean rate-of-strain tensor, defined as:

$$S \equiv \sqrt{2 S_{ij} S_{ij}} \tag{13}$$

$$S_{ij} = \frac{1}{2}\left(\frac{\partial \overline{U}_i}{\partial x_j} + \frac{\partial \overline{U}_j}{\partial x_i}\right) \tag{14}$$

The quantities α_k and α_ε are the inverse effective Prandtl numbers for k and ε respectively. The effective viscosity is computed using the high Reynolds number:

$$\nu_t = C_\mu \frac{k^2}{\varepsilon} \tag{15}$$

R_ε represents an additional source in the transport equation of the dissipation-rate and it is defined as:

$$R_\varepsilon = C_\mu \frac{\eta^3 (1 - \eta/\eta_0)}{1 + \beta\eta^3} \frac{\varepsilon^2}{k} \tag{16}$$

$$\eta = S \frac{k}{\varepsilon} \tag{17}$$

This additional term rends the RNG k-ε model more responsive to the effects of rapid strain and streamline curvature than the standard k-ε model, which explains the superior performance of the RNG model for certain classes of flows. The RNG k-ε version used is that of Yakhot and Orszag [30]. The model coefficients in the RNG k-ε model are:

$(C_\mu, C_{1\varepsilon}, C_{2\varepsilon}, \alpha_k, \alpha_\varepsilon, \eta_0, \beta) = (0.0845, 1.42, 1.68, 1.393, 1.393, 4.38, 0.012)$ (18)

3.2.2 Near-wall modelling

The RNG k-ε turbulence model described above is valid mostly for flows with a high Reynolds number. Correct calculation of a wall-bounded flow and its associated transport phenomena is not possible without an adequate description of the flow in the near-wall region where droplet deposition and evaporation occur. There are two approaches making it possible to take into account the viscous

effects near solid boundaries: the wall functions and near-wall modelling. In the so-called wall-function approach, a set of semi-empirical formulae using the classical logarithmic laws of the wall are applied to bridge the viscosity affected region. This technique allows important computational savings, as within this method, the near-wall region is not resolved, instead, it is linked via the wall functions. Unfortunately, the wall functions were initially created for simple shear flows [31]. For wall jets, the viscous layer plays an important role in heat and momentum transfer, especially in the transitional region before reaching similarity velocity profiles. Ljuboja and Rodi [32] had shown that for two-dimensional turbulent wall jet, the use of wall laws produces a spreading rate more than 30% higher than the experimental results. In addition, the flow separation and subsequent reattachment process generates extremely complex flow and heat transfer characteristics.

The "near wall modelling" approach uses modified turbulence models in the viscosity-affected region, and they are resolved with a mesh all the way to the wall. These models, which are not associated with wall laws, made it possible to predict effectively the dynamic and thermal characteristics of isothermal and non-isothermal turbulent wall jets [33]. Although the near-wall modelling approaches are more expensive in terms of computational times and memory requirements due to the fine meshes needed near the wall boundaries, their superiority has been established for complex flows including separation, reattachment points and re-circulation flows where the effects of wall-proximity are not well reflected by the classical logarithmic laws of walls [25,34]. Another reason justifying the use of near-wall modelling is due to the low velocity of the wall jet used in the present study which in turn implies low y^+ values near the walls. In this case, the use of standard wall function leads to relatively large first cells near the external walls of the RDC where the corresponding $y+$ should be at least equal to or higher than 30 to overcome the viscous sublayer zone [31]. This leads to a relatively coarse and inappropriate grid to capture local recirculations which are expected to occur downstream the inlet and the step.

In order to overcome the wall-functions limitations, the RNG k-ε was used in conjunction with the so-called ‘‘enhanced wall treatment’’ which guaranteed the correct asymptotic behaviour for large and small values of y^+ and reasonable representation of velocity profiles in the cases where y^+ falls inside the buffer region. This near-wall modelling method combines the two-layer model with enhanced wall functions. Therefore, the whole domain is subdivided into a viscous-sublayer region and a fully turbulent region. In the fully turbulent region the RNG k-ε model was used. In the viscous-sublayer region, a one-equation turbulence model based on the solution of the equation governing the kinetic energy of turbulence due to Wolfstein [35] in the immediate wall vicinity (near-wall layer). The demarcation of the two regions employing the modified Gibson and Launder [36] method is determined by a wall-distance-based turbulent Reynolds number, Re_y, which is defined as: $Re_y = k^{½}\, y/\nu \cong 200$, with k and y being the kinetic energy of turbulence and wall distance, respectively. The turbulent viscosity of the two regions was obtained from a single wall law by blending the linear (viscous sublayer) and logarithmic (turbulent) laws governing the wall using a function suggested by Kader [37]. The mean velocity at the walls is calculated as follows:

$$u^+ = e^{\Gamma} u_{vis}^+ + e^{1/\Gamma} u_t^+ \tag{19}$$

Where Γ is define by Kader [31] as a function of y^+ and wall roughness.

$$u_{vis}^+ = y^+, u_t^+ = \frac{1}{\kappa} \ln(Ey^+) \tag{20}$$

In this equation, $E = 9.793$.

The k equation is solved in all cases in the whole domain, using for the walls $\partial k / \partial n = 0$ where n is the local coordinate normal to the wall. The production of kinetic energy, and its dissipation rate ε, at the wall-adjacent cells, which are the source terms in the k equation, are computed on the basis of the local equilibrium hypothesis.

In this study, the both enhanced wall treatment and the classical logarithmic laws of walls were used. Comparisons with experimental data allow a critical evaluation of the performance of these near-wall modelling approaches. Unless otherwise stated, the results presented are related to the enhanced wall-treatment approach.

3.3 Mist flow model

Concerning the implementation of mist flow in the numerical model two complementary approaches were used a single and two-phase flow.

3.3.1. Single- phase flow

In this simplified approach, built with single-phase flow, saturation of the whole product surface in the cabinet is assumed ($(Hr)_{sat}$ = 100%). This means that locally on the surface of the products, the flow rate of the droplet deposit was higher or equal than the evaporating flow rate. In this case, the evaporating flow rate of water is not limited by impacted droplets flux and therefore it is governed by the difference between the water vapour content of the saturated air at the product surface temperature $(\omega_{T_S})_{sat}$ and at the air control volume next to the product surface located within the viscous sublayer of the air curtain $(\omega_{T_{air}})$.

$$\dot{m}_e = (\dot{m}_e)_{\max} = h_m \rho_a ((\omega_{T_s})_{sat} - \omega_{T_{air}}) \tag{21}$$

Where h_m represents the mass transfer coefficient of the water flux.

This simplified approach made it possible to evaluate locally the highest effectiveness of mist flow in terms of surface temperature decrease, since maximal values of $\dot{m}_e$ are considered with respect to airflow and the thermal characteristics of the air curtain. However, this approach was not able to compute the deposition of droplets along the RDC as function of inlet injection and local airflow pattern inside the cabinet. These aspects necessitate the use of the two-phase approach.

3.3.2. Two-phase flow

3.3.2.1. Two-phase model without droplet evaporation

A Lagrangian-formulated approach for two-phase flow is used to model the transport of droplets and their deposition in the modelled domain. The underlying concept here is what is usually called the dispersed two-phase flow. The idea is to consider one of the phases (droplets) to be dispersed in the continuous phase (turbulent airflow). The discrete phase model (DPM) option in Fluent solves the equation of motion for a discrete phase dispersed in the continuous phase, by adopting a Lagrangian frame of coordinates and leading to the computation of the particle trajectories. The motion of each particle of the dispersed phase is governed by an equation that balances the mass-acceleration of the particles with the forces acting on it. Appropriate forces such as the drag and gravitational forces have been incorporated into the equation of motion. For a particle of density ρ_p and diameter d_p, the governing equation is:

$$\frac{dU_i^p}{dt} = F_D (U_i - U_i^p) + \frac{(\rho_p - \rho)}{\rho_p} g_i \tag{22}$$

Here, U_i is the instantaneous air velocity and $(U_i = \overline{U_i} + u_i)$, U_i^p is the particle velocity. The second term on the right hand side of Eq. (22) is the buoyancy force. The first term on the right hand

side of Eq. (17) is the drag force per unit particle mass and F_D is dimensionally the inverse of time and reads:

$$F_D = \left(\frac{18\nu}{Sd_p^2}\right)\frac{C_D \mathrm{Re}_p}{24} = \frac{1}{\tau}\frac{C_D \mathrm{Re}_p}{24} \tag{23}$$

In this equation, τ is the particle relaxation time given as:

$$\tau = \frac{Sd^2}{18\nu} \tag{24}$$

S is the ratio of particle density to fluid density, d_p the particle diameter, C_D is the drag coefficient and Re_p is the Reynolds number for the particle referred to the relative velocity, which is defined as:

$$\mathrm{Re}_p = \frac{\rho d_p \left|U^p - U\right|}{\mu} \tag{25}$$

There are many models that can be used to determine the drag coefficient, but they are generally empirical. The polynomial model is one of the most commonly used models and is defined by:

$$C_D = a_1 + \frac{a_2}{\mathrm{Re}_p} + \frac{a_3}{\mathrm{Re}_p^2} \tag{26}$$

where a_1, a_2,and a_3 are constants that apply for smooth spherical particles over several ranges of *Re* given by Morsi and Alexander [38]. A particle trajectory is obtained by the solution of the particle momentum equation Eq. (22) coupled with the kinematic equation:

$$\frac{dx_i}{dt} = U_i^p \tag{27}$$

where x_i is the position coordinate of the particle at time t. The computed particle trajectories are combined into the source term of momentum. The momentum transfer from the continuous phase to the dispersed phase is equal to the change in momentum of droplets passing through each control volume as follows:

$$S_i^p = \sum_{trajectories} \frac{3\nu C_D \mathrm{Re}}{4\rho_p d_p^2}\left(U_i^p - U_i\right)\dot{m}_p \Delta t \tag{28}$$

where $\dot{m}_p$ is the mass flow rate of the dispersed phase (Kg/s) and Δt is the time step (s). This momentum exchange appears as a momentum sink into the right-hand side of the continuum phase momentum balance (Eq. 5).

Moreover, in turbulent flows, particle trajectories are not deterministic and two particles injected at a single point at different times may follow separate trajectories due to the random nature of the instantaneous fluid velocity. To account for the influence of turbulent fluid fluctuations on particle motion, a stochastic model, the discrete random walk (DRW) or "eddy lifetime" model, predicts the turbulent dispersion of particles by integrating the trajectory equations for each particle by adopting the instantaneous fluid velocity along the particle path. The fluid velocity in that space position where the particle is located, is:

$$U_i = \overline{U}_i + u_i \tag{29}$$

where $\overline{U_i}$ is the mean fluid phase velocity and u_i is the turbulent part of the fluid velocity. The DRW model assumes a Gaussian probability distribution. Because of the isotropic nature of the RNG k–ε model, the fluctuating velocity components u_i are equal in each direction and are proportional to the square root of the turbulent kinetic energy:

$$u_i = \xi_i \sqrt{2k/3} \tag{30}$$

where ξ_i is the normally distributed random number, which is taken as constant over the solution advancement time step related to Eq. (22) that cover the eddy time scale τ_e or "eddy lifetime":

$$\tau_e = 0.15\, k/\varepsilon \tag{31}$$

When the eddy lifetime is reached, a new value of the instantaneous velocity is obtained by applying a new value of ξ in Eq. (30). By replacing the mean velocity $U_i = \overline{U_i} + u_i$ in Eq. (22), each trajectory could interact with the modelled flow at each time step.

Particle trajectories were calculated repeatedly using the randomised turbulence until an average pattern of deposition was established. For these studies, the number of particles tracked was 10^4. This makes it possible to obtain at least one particle deposit on each cell on the product surface. Here, since the size of the particles was small ($\tau \ll 1$), the particles acted like fluid traces; thereby the prediction results of the air flow velocity and turbulence strongly affected the droplet trajectories and their deposition. For the DPM model, the initial conditions for the particles, such as initial position, velocity, diameter and number of the particles, are required.

3.3.2.2. Two-phase model with droplet evaporation

In this study, an original UDF was performed and built into the CFD numerical model in order to compute the deposited droplets while taking into account the evaporated flux part as given in the (Eq. 21) according to the surface temperature, the corresponding saturated water fraction and the water fraction in the first air control volume next to the solid surface.

The flow chart computational procedure related to the UDF was given in the Figure 2. This UDF makes it possible to compute cell by cell on the RDC surface the impinged droplet flux $\dot{m}_i$ as given in standard DPM procedure, the evaporated flux ($\dot{m}_e$), and finally the actual deposited flux ($\dot{m}_d$) which represents the excess water.

3.3.2.3. Two-phase model assumptions

Concerning the discrete phase introduced by droplet injection in the air curtains, the following hypotheses were assumed in a Euler-Lagrange approach:

- droplets were spherical and had the same diameter,
- droplets were uniformly injected into the flow field onto the whole surface of the holes with the same velocity as the inlet air,
- droplets did not reflect on wall boundaries. This means that all impacted droplets were trapped without rebound and recorded as deposited. Resuspension of deposited particles was not considered.
- droplets-droplets interactions are neglected. This means that droplets are assumed not to break up or coagulate,
- any change in the flow turbulence caused by the particles is not accounted for,
- droplets did not exchange heat or mass along their trajectory before impinging the products. This assumption was successfully used by Allais and Alvarez [19] in a similar mist-flow configuration could be partially explained by the saturation of air at the inlet. On the other hand, it should be noted that the mist flow process investigated in this study aims to maintain a quasi-saturated state on the product surface. In this case, it can easily be verified that heat and mass transfer between mist flow with a saturated surface and higher temperature surface maintain the saturation state of the air. Under steady-state conditions, heat and mass transfer between a mass flow rate $\dot{m}$ at temperature T_1 over a saturated surface ($L\ dx$) at temperature T_2 , higher than T_1, could be expressed as:

$$\dot{m}\ Cp_a\ dT = h\ (T_2 - T_1)\ L\ dx \quad (31)$$

$$\dot{m}\ d\omega = \rho\ h_m\ ((\omega_{T_2})_{sat} - (\omega_{T_1})_{sat}\ L\ dx \quad (32)$$

Where h and h_m represent the heat and mass transfer coefficients respectively.

For dilute gas mixtures such as the air and water vapour at near-atmospheric conditions, the heat transfer and mass transfer coefficient can be related by Chilton–Colburn analogy and can thus be expressed simply in terms of the Lewis number [39] as:

$$\frac{h}{h_m} = \rho \; Cp_{\;a} \; Le^{\;2/3} \tag{33}$$

Since the Lewis number in the mixture of air and water vapour is close to 1 in general, the following relation is obtained from 31 and 32.

$$\frac{d\,\omega}{dT} = \frac{1}{Le^{\;2/3}} \frac{d\,\omega_{sat}}{dT} \approx \frac{d\,\omega_{sat}}{dT} \tag{34}$$

where Le and Cp_a are the Lewis number and specific heat of dry air, respectively. Equation 34 indicates the maintaining of saturated state of air over the saturated surface.

3.4. Boundary conditions

The 2-D computational domain is obtained from a cross-section of the cabinet, including a larger portion of the external ambient both in transversal and longitudinal directions. This further extension is required in order take into account the exchanges between the air curtain and the surrounding air. In addition, this extension should be sufficiently large so that the external boundaries do not have any influence on the flow of the air curtain. The numerical solution precision strongly depends on the accuracy of the boundary conditions and the way in which these conditions are integrated within the numerical model. Figure 3 shows the geometry of the cabinet and the boundary conditions used for the calculations. In our case, the following boundary conditions were considered:

- at the RDC inlet, the distributions of velocity, temperature, turbulence and water mass fraction are assumed to be uniform. In this two-dimensional configuration, the actual circular holes were represented by uniform rectangular slots with the same open sections and the same inlet velocity. Therefore, the air-supply unit is equally divided into 10 slots resulting in a total inlet surface of 0.022 m2. The velocity and temperature values are given as known values using the experimental data: U_0 = 2 m.s^{-1}, T_0 = 272 K. This gives rise to a total mass flow rate of: $\dot{M}_0 = 0.057 \;\; kg \;/\; s$. Concerning the turbulence quantities, they are imposed by means of two parameters, the turbulence intensity defined as the ratio of RMS flow velocity fluctuations to the mean flow velocity and the slot's hydraulic diameter. The turbulence quantity intensity was assumed to be 5%. However, the initial turbulent kinetic energy, is relatively small compared with that generated by the multi-slotted jets and therefore flow pattern and final droplet deposition results should not be very sensitive to the inlet turbulence parameters provided they are of the correct order.

- at the outlet, velocity is computed and imposed with respect to the RDC mass balance and zero-gradient was applied for all transport variables normal to flow direction. This means that a fully developed flow is assumed, whose velocity profile and other properties remain unchanged in the flow direction.

- on the two "opening boundaries" bordering the modelled domain, a small and uniform pressure jump was applied. This condition allowed the air to enter the domain through one boundary at the imposed ambience temperature (T_a = 298 K) and to exit through the other at the mixing temperature.

- on the floor and the ceiling, and all the walls related to the cabinet, zero velocity, zero heat flux and zero water flux are assumed.

Convective and radiative effects were considered on the product surface which were modelled as a black body, with an uniform emissivity (ε_a=1). This assumption enables comparison with experimental data concerning product surface temperature obtained with a black painted sensors. The internal conduction within products was neglected as respect to insulated medium used in experiments. A source term was applied on the RDC product surface. It takes into consideration the radiative and the latent evaporative heat flux induced by the mist flow. It can be expressed as:

$$S_\phi = (\Phi_r)_{net} - \Phi_e = ((\Phi_r)_i - \sigma T_s^4) - \Phi_e \quad (35)$$

$$\Phi_e = \dot{m}_e \, Lv \quad (36)$$

Where $(\Phi_r)_i$ was obtained from radiative heat transfer measurements.

Therefore, the thermal boundary condition on the RDC also reflected the heat balance on the RDC surface and can be expressed as:

$$(\Phi_r)_{net} - \Phi_e = \phi_{conv} = h_c (T_a - T_s) \quad (36)$$

To solve this set of equations related to RDC surface, heat and mass exchanges were calculated cell by cell using the temperature and concentration profile in the air control volume next to the product surface. With respect to the enhanced wall treatment procedure, the near-wall mesh must be fine enough to resolve the transport equations down to the viscous sub-layer ($y^+ \sim 1$). The maximal value of evaporated flux used in the single-phase approach (Eq. 16) can be expressed as:

$$(\dot{m}_e)_{\max} = h_m \rho_a ((\omega_{T_s})_{sat} - \omega_{T_a}) = \rho_a D_m \frac{((\omega_{T_s})_{sat} - \omega_{T_a})}{d_{cell}} \quad (37)$$

$$\Phi_c = h_c (T_a - T_s) = \frac{\lambda_a (T_s - T_a)}{d_{cell}} \quad (38)$$

Where d_{cell} represents the distance from wall to the adjacent cell control volume.

3.5 Configurations studied

The spatial characteristics of the aerodynamic interactions between droplets and air curtain are critical for the process. In order to characterize the influence of these interactions on the droplet transport and deposition, four droplet inlet configurations were investigated: High injection configuration (HIC), Medium injection configuration (MIC), Bottom injection configuration (BIC) and Global injection configuration (GIC). For HIC, MIC, BIC and GIC, droplets are injected at the highest three inlet slots, the four medium inlet slots, the three bottom inlet slots and at the total ten inlets slots respectively.

3.6 Numerical resolution

The computations were carried out using FLUENT, a commercial computational-fluid dynamics (CFD) code with a two-dimensional configuration. The governing equations are solved using the finite-volume method in a staggered grid system. The geometrical model and the computational grid were created using Fluent's Gambit pre-processing tool. A non-structured and non-uniform mesh with a growth factor less than 1.2 were used. The mesh was generated with quad and pave scheme. Near the product surface, hexahedral cells were used to allow the wall jet flow to be aligned with the mesh and therefore to minimize the numerical diffusion. The thinner cells were located in the high-velocity gradients zones, i.e. in the air curtain and particularly near the inlet and outlet areas jets. The numerical results are obtained with 12 200 cells. It was observed that increasing the grid to larger than 10 000 does not affect the numerical results. A view of the used mesh inside the cabinet is given in the Figure 4.

The well-known SIMPLE algorithm was used for coupling pressure and velocity into the continuity equation. The second-order upwind differencing scheme was used for the convection terms of flows and all transported variables to reduce the numerical diffusion. The second-order central-differencing scheme was used for diffusion terms.

Concerning the two-phase flow case, velocity and trajectory calculations for the particles can be treated both as uncoupled or as coupled with the continuous fluid field solution. Obviously, the second option requires iterations between each set of balance equations. This option is useful in the case where discrete phase injection is such that feedback on the fluid field quantities (e.g. velocity, pressure) is expected. Otherwise, the segregation between the two solutions is acceptable. The steady-state analysis is carried out through the following steps: (i) solving of the continuous phase flow; (ii) injection of the discrete phase; (iii) solving of the coupled flow and particle trajectories. This two-way coupling is accomplished by alternatively solving the discrete and continuous phase until the convergence criteria are met in both phases; (iv) tracking of the discrete phase.

Particle trajectories were calculated repeatedly using the randomised turbulence until an average pattern of deposition was established. For these studies, the number of particles tracked was 10^4. This allows at least one deposited particle on each cell on the product surface.

4. Results and Discussion

Figure 5 shows the evolution of the heat radiative incident flux along the exposed surface of the cabinet obtained experimentally by the radiative probe. The overall trend shows a slight decrease along the RDC due to the influence of the protecting glass, colder than the surrounding walls. This figure also shows that lower values of the heat radiative incident flux were obtained just downstream the inlet and the middle step, due to the proximity of the corresponding elevated colder walls of the RDC. This aspect highlights the local effect of view factors due to the internal topology of the RDC. However the difference between the lower and higher values did not exceed 10%. It's good to notice that the higher value (432 W/m2) was close to the theoretical value of $\sigma T_{wall}^{4} \cong 447\ w/m^2$ in case of radiative exchange between a small object placed inside a large cavity assumed to be maintained at a uniform temperature of about ($T_{wall} = Ta = 298$ K).

Figure 6 presents a comparison between numerical and experimental data concerning the contours of iso-velocity magnitude in the air curtain. The experimental results were obtained by interpolation of 244 measurement points. This comparison showed qualitative good agreement on the overall behaviour of the airflow pattern of the air curtain related to primary and secondary flows. This concerns the jet deviation, the location of its attachment on the products surface at $x \sim 0.22$ and $x \sim 0.67$, the longitudinal extent and the aerodynamic intensity of the two clockwise recirculation areas located downstream from the step and just below the inlet grid, which are mainly pressure gradient driven flows. Figure 6b also shows in the inlet area the aerodynamic behaviour of multi-slotted jets tending to intersect with each other and to combine by local depression into a single overall jet before being attached by the Coanda effect onto the product surface. This phenomenon was similar to that observed by Moustafa [40] in a study concerning the behaviour of multi-slotted jets downstream the nozzle exit.

Figure 7 compares predicted and measured vertical velocity profiles located at x = 0.05, 0.3, 0.6 and 0.75 m from the inlet section located upstream and downstream the step (x = 0.5 m). This figure also showed the ability of the numerical model to accurately predict the local characteristics of the flow developed along the cabinet. This concerns the overall velocity profile shape, the maximum velocity values and their local positions, suggesting an accurate prediction of the longitudinal and vertical expansion of the jet along the cabinet. It also concerns the magnitude and the extent of the reverse flow observed within recirculated areas in the lower part of the profiles: x = 0.05 and 0.6 m. On average, an accuracy of 10% is obtained for the velocity magnitudes.

Figure 8 presents a comparison between computed and experimental data concerning the evolution of the dimensionless surface temperature ($T^* = (T_s - T_0)/(T_{s\max} - T_0)$) along the cabinet. In order to illustrate the importance of the near-wall treatment, numerical values are computed using near-wall enhancement and the classical logarithmic walls. Although the complexity of the flow including separated flows, an overall good agreement between the calculated with enhanced wall treatment procedure and the measured surface temperatures can be observed. This concerns the overall trend along the cabinet and the extreme values obtained locally within the recirculated areas where the jet is detached, which leads to a rise in the surface temperature and on reattachment points where lower temperatures are obtained locally. The differences between calculated and measured values were within 1.5 K. The higher temperature was obtained downstream the step at x = 0.55 m where the jet is detached. Besides this local position, higher temperatures were also obtained near the outlet section. This trend confirmed experimental data obtained by other authors on similar cabinets [3, 10]. On the other hand, the use of the logarithmic wall laws implies higher discrepancies with experimental values especially within separated flows. The largest difference occurs in inlet area at x~ 0.015 m and could be probably amplified by the conjugated effect of the transitional and separated flow aspects. Overall, this comparison also underlines the superiority of enhanced wall treatment based on $Re_y \equiv k^{½}\, y/\nu$ over the classical logarithmic laws based on $y+ \equiv u_\tau\, y/\nu$ in predicting the near-wall thermal behaviour in transitional complex flows including separated and reattaching regions. Obviously, in these regions the wall shear stress cannot be clearly defined and the law governing the wall is no longer applicable.

Figure 9 shows the evolution of experimental and numerical data related to the net radiative exchange on the exposed surface of RDC. The experimental values were obtained by the relation: $(\phi_r)_{net} = (\phi_r)_i - \sigma T_s^4$). According to the assumptions made on the model leading to neglecting the heat transferred by conduction through the products considered as insulated medium, the net radiative part also represents the heat exchanged by convection on the considered surface. This means that the good agreement obtained between numerical and experimental data observed in this figure, also reflects an appropriate prediction of convective heat transfer exchanges within the wall jet along the product surface in bulk and near-wall regions.

4.1. Mist cooling with single-phase flow

In order to illustrate the mist cooling effect, Figure 10 presents a comparison of the evolution of surface dimensionless temperature ($T^* = (T_s - T_0)/(T_{s\max} - T_0)$) of the two limiting cases obtained with and without mist flow. The latter case was obtained with the single-phase flow approach by assuming a saturated product surface, which means that there are enough deposited droplets to cover the entire surface. This curve also reveals the highest mist cooling effect that could be obtained with this process along the RDC surface since maximal values of $\dot{m}_e$ are locally considered (Eq. 21). The results show that mist cooling makes it possible to decrease the higher temperatures by approximately 24 % and this corresponds to 3 K**.** The same order of magnitude was also obtained experimentally using water-saturated plaster slabs in which free evaporation on their surface is assumed (a_w = 1). This methodology was successfully used by many authors to simulate food refrigeration with a wetted surface [41-42]**.** Numerical and experimental values also show that the effectiveness of mist cooling increases with increasing surface temperature levels which is in accordance with Eq. (21).

4.2. Two-phase model: aerodynamic study of droplet deposit without evaporation

Figure 11 presents the numerical results concerning the evolution of the droplet deposit rate along the RDC product surface obtained with GIC, for different mass droplet flow rate $\dot{m}_0 = 1\,10^{-04}$, $5\,10^{-05}$ and $3\,10^{-05}\, kg/s$ yielding 0.17, 0.085 and 0.053% for mist concentrations ($\dot{m}_0 / \dot{M}_0$) respectively. This figure shows that a higher value of deposited droplets was obtained near the attachment point of the jet (x ~ 0.2). Then, the air flow behaves as a wall jet and the corresponding

droplet deposit exhibits a strong decay along the RDC surface until x < 0.5. A similar trend was also observed by Li et al. [20] downstream from the jet stagnation point related to heat transfer enhancement caused by droplet interaction with the target wall. On the contrary, the lower values of droplet deposit in Figure 8 are observed within recirculated areas located near the inlet (x < 0.2) and downstream from the step (0.5< x <0.6) due to the detachment of the jet. In these separated-flow areas, convection could be neglected and transport droplet mechanisms are only governed by diffusion. The presence of an upward velocity in the re-circulated flows also tends to decrease the deposit mechanisms in these areas. This result is also confirmed by Figure 12 which represents numerical data of the droplet concentration within the air curtain for where lower concentration values are observed within recirculated areas. In the downstream part of the RDC (0.5< x < 1) where more fully developed flow takes place for which convection and diffusion are of the same order of magnitude, more uniform values of droplet deposit are observed.

Overall, the deposit distribution was not well correlated with the temperature distribution and therefore with the local need for mist cooling. For example, 80% of the collected droplets on the RDC surface were located in the upstream part of the RDC (x <0.5), which represents the coldest area and 20% in the downstream part where higher temperatures are expected (Table 1). On the other hand, the use of different mass droplet rates does not modify this trend since the corresponding droplet deposit curves are similar. This could be explained by the lower diameter of droplets and lower mist concentrations values for which the drag effect and therefore the momentum exchange with the continuum phase could be neglected [38]. This finding highlights the importance of a better control of the droplet injection configuration in order to qualitatively modify the spatial distribution of droplet deposit as respect to the local surface temperature.

In order to optimise the mist flow process, the three configurations presented above obtained with bottom, medium and high droplet injection, are investigated and compared to the global injection presented in Figure 11. These comparisons, obtained with $\dot{m}_0 = 1\,10^{-04}\ kg/s$, are presented in terms of droplet concentration within the air curtain (Figure 13) and the evolution of the droplet deposit along the RDC (Figure 14). For the same configurations, table 1 summarizes the data relating to the ratio of collected droplets on the RDC to the total water mass flow rate ($\dot{m}_0 = 1\,10^{-04}\ kg/s$) and to the collected droplet rate at the upstream part (0<x <0.5), the downstream part (0.5 <x <1) and the whole cabinet surface.

These results clearly indicate that transport and deposition of droplets are significantly affected by the locations of injection point. The highest deposit ratio for the whole cabinet was observed in bottom injection configuration (BIC). This ratio is equal to 20% and represents 2.3 10^{-5} kg/s of the total droplet flow rate ($\dot{m}_0 = 1\,10^{-04}\ kg/s$). In comparison with GIC, this increasing in droplet deposit (20% for BIC instead of 18% in GIC) is not well correlated to the local need in mist flow because the majority of impinged droplets are collected in the upstream part of the RDC upstream the step which represents the coldest area. This could be easily explained by the proximity of the injection points to the upstream part of the cabinet as seen in Figure 13 a. On the contrary, the use of a high injection configuration (HIC) results in a lower deposition ratio (0.2%). This could be easily explained by the remoteness of the highest distance separating the injection point from the RDC surface. In this case, the majority of droplets are disseminated in the ambience and only a small amount is captured by the RDC. FOR BIC and HIC, the corresponding Figures 13 a and 13 c qualitatively confirm these trends. The same observation was demonstrated by Sun et al. [26] in a study concerning the dispersion and settling characteristics of droplets in a ventilated room. The results clearly indicate that for small droplets a lower initial position of the source of droplets in the room results in a higher deposition rate of the droplets on the floor.

Finally, the use of a medium injection configuration (MIC) seems to qualitatively improve the process. In contrast to GIC and BIC, the droplet deposition curve obtained with MIC differs substantially in shape. Obviously, the use of medium droplet injection causes more uniform and gradual transverse diffusion within the air curtain and thus avoids direct interaction between droplets and the RDC

surface (Fig. 13b). In this case, the droplet deposition mechanism is governed more by turbulence and small scale diffusion within the core jet than by impingement which involves larger convective scales at the jet boundaries. As a consequence, the droplet deposition obtained with MIC exhibits a gradual increase in the upstream RDC's part followed by a quasi-uniform values in the downstream RDC's part. In addition, the peak value observed near the jet attachment in GIC and BIC is considerably delayed since lower droplet concentration is present in the jet boundaries in this area. This configuration considerably increases the rate of captured droplets in the downstream part of the RDC where the higher temperatures are observed, while reducing droplet deposition in the upstream part where lower temperatures are located.

4.3. Mist cooling using two-phase flow

In order to assess the effectiveness of the global and the medium injection configuration in terms of droplet deposition and temperature decrease, different simulations were performed with the home made UDF. Figure 15 compares the surface temperature on a RDC obtained with $\dot{m}_0 = 2.2\,10^{-05}\,kg\,/\,s$ using GIC with to the two limiting values of surface temperature presented above in Figure 10.

The non-uniformity of the temperature decrease reflects the heterogeneity of the spatial distribution of droplet deposition. The higher temperature decrease in the upstream part of the RDC contrasted with the lower temperature decrease obtained in the downstream part. The dimensionless temperature decrease reaches its maximal value of 0.15 at $x \sim 0.18$ and only 0.03 at $x \sim 0.85$. In this figure, the water mass flow rate ($\dot{m}_0 = 2.2\,10^{-05}\,kg\,/\,s$) used for this simulation was optimised by trial and error with UDF in order to reach the highest value that can be used with GIC, while avoiding excess water on the RDC surface. As it can be observed, the surface temperature obtained with $\dot{m}_0 = 2.2\,10^{-05}\,kg\,/\,s$ reached the minimal temperature obtained with saturated surface at $x \sim 0.18$. This position corresponds to the peak of collected droplets observed in Fig. 11 related to GIC. It is noteworthy that using a water mass flow rate that is higher than $\dot{m}_0 = 2.2\,10^{-05}\,kg\,/\,s$ leads to a higher temperature decrease in the downstream part of the RDC. But in this case, excess water is locally unavoidable especially near the attachment point area ($x \sim 0.18$), where deposited droplets could overcome the maximal flux evaporated rate $(\dot{m}_e)_{\max}$ defined in Eq; (21). This aspect considerably limits the global performance of the mist-cooling process in the GIC case and underlined the major drawback of this configuration.

Figure 16 displays the surface temperature in an RDC obtained with $\dot{m}_0 = 1\,10^{-04}\,kg\,/\,s$ and $\dot{m}_0 = 2.6\,10^{-04}\,kg\,/\,s$ using MIC. These curves were compared with the two limiting values of surface temperature presented above in Figure X. In comparison with the HIC, the use of MIC makes it possible to use higher water flow rate, and therefore to enhance the temperature decrease while avoiding excess water. The use of $\dot{m}_0 = 1\,10^{-04}\,kg\,/\,s$ makes it possible to decrease by 1 K the temperature levels in the upstream part as well as in the downstream part of the RDC. On the other hand, numerical simulations were performed with UDF in order to reach the higher water flow rate that can be used with MIC without causing excess water on the RDC surface. This was obtained with $\dot{m}_0 = 2.6\,10^{-04}\,kg\,/\,s$, which makes it possible to decrease by 0.23 % (2.8 K) the higher dimensionless temperature near the outlet area of the RDC. In this case, the limiting point is located at the end of the upstream part of the RDC ($x \sim 0.45$) where the temperature obtained with $\dot{m}_0 = 2.6\,10^{-04}\,kg\,/\,s$ reaches the maximum local cooling enhancement which corresponds to the saturation surface.

4.4. Experimental investigations with two-phase approach

Figure 17 presents surface temperature measurements made on the downstream part of the RDC obtained, without mist flow and with mist flow with MIC using two droplet flow rates: $\dot{m}_0 = 1.1\,10^{-04}\,kg/s$ and $\dot{m}_0 = 1.7\,10^{-04}\,kg/s$. The corresponding temperature decreases were 12 % (1.4 K) and 22 % (2.3 K) respectively. This trend was in line with predicted values displayed in Figure 16. In addition, the temperature decrease of 2.3 K obtained with the higher droplet flow rate ($\dot{m}_0 = 1.7\,10^{-04}\,kg/s$) was of the same order of magnitude as theoretical value obtained with single-phase flow. However, it was not possible to explore the effectiveness with a higher mass flow rate since we use the mist generator at its maximal capacity. Other results not shown here show that for $\dot{m}_0 = 1.7\,10^{-04}\,kg/s$ the cooling enhancement is limited to 1.1 K for BIC. Qualitatively, this clearly agrees with numerical values regarding the superiority of MIC over BIC.

These experimental results for temperature decrease also reveal a slight underestimation of numerical values: (1.4 K for $\dot{m}_0 = 110^{-04}\,kg/s$) and (2.3 K for 1.62 10^{-04} kg/s) obtained experimentally instead of (1 K for m = $\dot{m}_0 = 110^{-04}\,kg/s$) and (2.8 K for $\dot{m}_0 = 2.6\,10^{-04}\,kg/s$) obtained numerically. This difference is above all due to the fact that experimentally, droplets are injected directly into the air curtain, 10 cm away from the inlet section. This configuration avoids the higher amount of turbulence generated by multi-slotted jets in the inlet area. This aspect limits droplet dispersion mechanisms in the inlet area, improves droplet transport and deposition further downstream at the end of the RDC and therefore could explain the higher values of temperature decrease obtained experimentally. On the other hand, the higher specific heat capacity of saturated mist flow than in the air expressed in Eq. (1), not considered in the model, could also explain these differences. Experimental values show that the temperature rise of the air curtain computed as the difference between $T_{outlet} - T_0$ was 4.4 K without mist flow and 2.4 K with mist flow using $\dot{m}_0 = 110^{-04}\,kg/s$. Qualitatively, this confirms the theoretical ratio of the corresponding heat capacity: $Cp_{\text{mist flow}}/Cp_{a} \sim 2$ given by the relation (1).

5. Conclusion

Numerical CFD approach and full-scale experiments were carried out in order to characterize the airflow pattern and the temperature levels on the surface of the products in an RDC configuration with and without mist flow.

In single phase-flow, the good agreement obtained between numerical and experimental data underlines the ability of the RNG turbulence to predict the aerodynamic and thermal behaviour of the air curtain in bulk and near-wall regions. This concerns the wall-jet attachment, recirculated areas, velocity profiles, the surface temperature and the convective heat transfer exchanges. This study also demonstrates the superiority of enhanced wall treatment based on $Re_y \equiv k^{½}\,y/\nu$ over the classical logarithmic laws based on $y+ \equiv u_\tau\,y/\nu$ in predicting the near-wall thermal behaviour in transitional flows including separated and reattaching regions.

In two-phase-flow, an original user-defined function was performed and built in a Lagrangian-formulated approach to compute the deposited droplets while taking into account the evaporative flux of droplets at the product surface. This makes it possible to optimize droplet injection in order to better control spatial distribution of droplet deposit as regards to the temperature heterogeneity on the RDC surface. The aim is to increase the droplet deposition in the higher temperature areas located downstream the air curtain and to decrease it in the coldest area located in the upstream part where water stagnation should be avoided.

In order to optimize the mist flow process, four inlet droplet injection configurations related to overall, high, bottom and medium position for droplet release at the inlet section of the air curtain were tested and compared. The comparisons between these configuration show that the location of droplet injection is the key factor controlling the spatial distribution of droplet deposit and therefore the effectiveness of mist flow process as regards to the local need for mist cooling on the RDC surface. Numerical results clearly indicate the better performance of the medium configuration which makes it possible to increase the droplet deposition in the higher temperature areas located near the outlet and to decrease it in the coldest area located near the inlet where water stagnation should be avoided. For MIC, the numerical results also show that as little as 0.4% of mist concentration ($\dot{m}_0 / \dot{M}_0$) that corresponds to $\dot{m}_0 = 2.6\,10^{-04}\,kg/s$, the mist flow process makes it possible to decrease the higher dimensionless surface temperatures by approximately X%, corresponding to 2.8 K. The same order of magnitude was obtained experimentally with mist flow.

The encouraging results obtained with the two-phase flow approach, suggest that that CFD model might be an appropriate tool to optimise the use of the mist flow process in more complex RDC configurations. However, further work is still required to assess the energetic impact of mist flow on the operating of the refrigerating unit in terms of frost and defrost cycles.

REFERENCES

1. Y.-G. Chen, X.-L. Yuan – Experimental study of the performance of single-band air curtains for a multi-deck refrigerated display cabinet. *Journal of Food Eng*. 69, 261-267 (2005).

2. J.N. Baleo, L. Guyonnaud, C. Solliec - Numerical simulation of air flow distribution in a refrigerated display case air curtain, *19th IIR International Congress of Refrigeration*, Proceedings Vol. 2, 681-687 (1995).

3. G. Cortella - CFD-aided retail cabinets design, *Computers and Electronics in Agriculture* 34, 43-66 (2002).

4. H. van Ort, R.J.M. Van Gerwen Air flow optimisation in refrigerated cabinets, *19th IIR International Congress of refrigeration*, Proceedings vol. 2, 446-453 (1998).

5. T.H. Lan, D.H.T. Gotham, M.W Collins - A numerical simulation of the air flow and heat transfer in a refrigerated food display cabinet, *2nd European Thermal-Sciences and 14th UIT National Heat Transfer Conference*, 1139-1146 (1999).

6. A.M. Foster, M. Madge, J.A. Evans – The use of CFD to improve the performance of a chilled multi-deck retail display cabinet, *International Journal of Refrigeration* 28, 698-705 (2005).

7. H.K. Navaz, B.S. Henderson, R. Faramarzi, A. Pourmovahed and F. Taugwalder - *Jet entrainment rate in air curtain of open refrigerated display cases. International Journal of Refrigeration* 28, 267-275 (2005).

8. D. Stribling, S.A. Tassou, D. Mariott – A two-dimensional CFD model of a refrigerated display case, *ASHRAE Trans Res*. 88-94 (1999).

9. J. Cui, S. Wang – Application of CFD in evaluation and energy-efficient design of air curtains for horizontal refrigerated display cases, *Int. Journal of Thermal Sciences* 43, 993-1002 (2004).

10. S. Bobbo, G. Cortella, M. Manzan - The temperature of frozen foods in open display cabinets: simulation and testing, 19th International Congress of Refrigeration, Proceedings, vol. 2, 697–704 (1995).

11. Pan Xueqin - Etude et modélisation d'un meuble frigorifique de vente (MFV) à haute efficacité énergétique, Thèse de l'Ecole des Mines (2000).

12. S.J. James, J. A. Evans, Temperatures in the retail and domestic chilled chain. *Processing and quality of foods, Chilled foods: the revolution of freshness*, vol. 3, Elsevier Applied Science Publishers, London, 3273- 3278 (1990).

13. C.O. Gill, T. Jones, A. Houde, D.I. Leblanc, K. Rahn, R.A. Holley, R. Starke – Temperatures and ages of packs of beef displayed in multi-shelf retail cabinets, *Food Control*, 145-151 (2003).

14. F.C. Hayes – Heat transfer characteristics of the air curtain: a plane jet subjected to transverse pressure and temperature gradient, PhD Thesis, University of Illinois, Urbana, IL (1968).

15. G. Rigot - Modélisation et simulation des meubles frigorifiques de vente fonctionnant dans des conditions variables, *20th IIR International Congress of Refrigeration*, Sydney, (1999).

16. G. Rigot - Interaction environnement et meubles de vente, *RPF*, 1996, n°835 53-56 (1996).

17. ASHRAE, *ASHRAE Handbook - Fundamentals*. American Society of Heating, Refrigerating and Air-Conditioning Engineers, Inc., (Chapters 5–6) (1997).

18. T. Brown, J.E.L. Corry, S.J. James. – Humidification of chilled fruit and vegetables on retail display cabinet using an ultrasonic fogging system with water/air ozonation. *International Journal of Refrigeration*, 27, 862-868 (2004).

19. I. Allais, G. Alvarez – Analysis of heat transfer during mist chilling of a packed bed of spheres simulating foodstuffs. Journal of Food Engineering, 49, 37-47 (2001).

20. X. Li, J.L. Gaddis, T. Wang – Mist/steam cooling by a row of impinging jets, *International Journal of Heat and Mass Transfer*, 46, 2279-2290 (2003).

21. T. Wang, J.L. Gaddis, X. Li - Mist/steam heat transfer of multiple rows of impinging jets, *International Journal of Heat and Mass Transfer*, 48, 5179-5191 (2005).

22. N.V. Nirmalan, J.A. Weaver, L.D. Hylton, An experimental study of turbine vane heat transfer with water-air cooling, ASME J. Turbomachin. 120, 50-62 (1998).

23. Yu. A. Buyevich, V. N. Mankevich - Cooling of a superheated surface with a jet mist flow, *International Journal of Heat and Mass Transfer*, 39, 2353 – 2362 (1996).

24. Liu Chaosheng, G. Ahmadi - Transport and deposition of particles near a building model, *Building and Environment*. 41, 828-836 (2006).

25. Z.F. Tian, J.Y. Tu, G.H. Yeoh, R.K.K. Yuen - On the numerical study of contaminant particle concentration in indoor airflow, *Building and Environment*, 41, 1504 – 1514 (2006).

26. Wei Sun, J. Lie, Y. Li, X. Xie - Dispersion and settling characteristics of evaporating droplets in ventilated room, *Building and Environment*, 42, 1011-1017 (2007).

27. S.T. Parker, R.P. Kinnersley – A computational and wind tunnel study of particle dry deposition in complex topography. *Atmospheric Environment* 38, 3867-3878 (2004).

28. N. Rajaratnam - Turbulent Jets, Elsevier, Amesterdam, (1976).

29. F. J. Trujillo, Q. T. Pham - A computational fluid dynamic model of the heat and moisture transfer during beef chilling, *International Journal of Refrigeration* 29, 998-1009 (2006).

30. V. Yakhot, S.A. Orszag - Renormalisation group analysis of turbulence, 1. Basic theory. *J. of Scientific Computing* 1, 3-51 (1986).

31. B.E. Launder, D.B. Spalding, The numerical computation of turbulent flows, *Computer Methods in Applied Mechanics and Energy* 3, 269-289 (1974).

32. M. Ljuboja, W. Rodi – Calculation of turbulent wall jets with an algebraic Reynolds stress model, *J. Fluids Engg*. 3, 267-289 (1974).

33. J. Kechiche, H. Mhiri, G. Le Palec, P. Bournot – Application of low Reynolds number k-ε turbulence models to the study of turbulent wall jets - *International Journal of Thermal Sciences* 43 201-211 (2004).

34. T.S. Park, H.J. Sung – A nonlinear low-Reynolds-number k-ε model for turbulent fseparated and reattaching flows – Flow field computations, *International Journal of Heat and Mass Transfer* 38 2657-2666 (1995).

35. M. Wolfstein - The Velocity and Temperature Distribution of One-Dimensional Flow with Turbulence Augmentation and Pressure Gradient. *Int. J. Heat Mass Transfer* 12, 301-318, (1969).

36. M.M. Gibson, B.E. Launder, 1978. Ground effects on pressure fluctuations in the atmospheric boundary layer. *J. Fluid Mech*. 86, 491–511 (1978).

37. B. Kader - Temperature and Concentration Profiles in Fully Turbulent Boundary Layers. *Int. J. Heat and Mass Transfer* 24, 1541-1544 (1993).

38. S.A. Morsi, AJ. Alexander – Investigation of particle trajectories in 2-phase flow systems. *Journal of Fluid Mechanics* 55, 193-208 (1972).

39. M.N. Özisik - *Heat Transfer, A Basic Approach*. McGraw-Hill International edition, (1985).

40. G.H. Moustafa – Experimental investigation of High-Speed Twin jets. *AIAA Journal*, vol. 32, n°11, (1993).

41. A. Kuitche, G. Letang and J.D. Daudin - Modelling of temperature and weight loss kinetics during meat chilling for time-variable conditions using an analytical-based method - II. Calculations versus measurements on wet plaster cylinders and cast. *J Food Eng.* 29, 85-107 (1996).

42. L. A. Campañone, S. A. Giner and R. H. Mascheroni - Generalized model for the simulation of food refrigeration. Development and validation of the predictive numerical method. *International Journal of Refrigeration 25, 975-98* (2002).

Acknowledgments

The authors would like to thanks the Ile De France Region and the French Ministry of Agriculture, for their financial support for this research project.

NOMENCLATURE

a_w	water activity
Cp	specific heat ($J.kg^{-1}.K^{-1}$)
C_i s	turbulence model coefficients
D_m	molecular diffusivity ($m^2.s^{-1}$)
h_c, h_r	convective, radiative heat transfer coefficient ($W.m^{-2}K^{-1}$)
h_m	mass transfer coefficient ($m.s^{-1}$)
L	Length of the cabinet (m)
L_v	latent heat of vaporization ($J.kg^{-1}$)
k	kinetic energy of turbulence ($m^2.s^{-2}$)
Le	Lewis number
$\dot{m}$	mass flow rate of discrete phase ($kg.s^{-1}$)
$\dot{M}$	mass flow rate of continuum phase ($kg.s^{-1}$)
p	pressure (*Pa*)
Pr	Prandtl number
P_k	production term ($m^2.s^{-3}$)
S_ϕ	Source term in the energy equation
S_i^p	Source term in the momentum equation
T, t	Mean, fluctuating temperature (K)
T*	Dimensionless temperature ($T^* = (T_s - T_0)/(T_{s\max} - T_0)$)
$\overline{u_i u_j}$	Reynolds stresses component ($m^2.s^{-2}$)
$\overline{U_i}$ u_i	mean and fluctuating velocity component in x_i direction ($m.s^{-1}$)
U_i	instantaneous air velocity

Greek symbols:

α	Thermal diffusivity ($m^2.s^{-1}$)
β	Thermal expansion coefficient (K^{-1})
δ_{ij}	Kronecker delta function
ε	turbulence energy dissipation rate (m^2s^{-3})
ρ	density ($kg.m^{-3}$)
ρ_0	Reference density of the air at T_0 ($kg.m^{-3}$)
σ	Stephan-Boltzmann radiation constant ($5.67x10^{-8}$ $W.m^{-2}K^{-4}$)
ε_a	Emissivity
λ	Thermal conductivity ($W.m^{-1}K^{-1}$)
ν	Kinematic viscosity ($m^2.s^{-1}$)
Φ	Thermal flux ($W.m^{-2}$)
ω_T	Water vapour content at temperature T (kg water/kg of dry air)

Indices

a	air
am	ambience
c	convective
d	deposited droplets
i	impinged droplets
p	particle
r	radiative
t	turbulent
e	evaporated droplets
s	surface
0	inlet
sat	saturation

Injection Configuration $\dot{m}_0 = 110^{-4} kg/s$	Impinged droplet rate(kg/s) = $\int_L \dot{m}_i dl$			Ratio of impinged droplets $\int_{L\in[0,1]} \dot{m}_i dl \Big/ \dot{m}_0$
	Upstream part of the cabinet: L∈[0,0.5]	Downstream part of the cabinet: L∈[0.5,1]	whole RDC surface: L∈[0,1]	
GIC	1.4 10^{-5}	3.2 10^{-6}	1.8 10^{-5}	18%
HIC	1.3 10^{-8}	2.2 10^{-7}	2.3 10^{-7}	0.2%
MIC	1.4 10^{-6}	1.9 10^{-6}	3.3 10^{-6}	3%
BIC	1.8 10^{-5}	4.8 10^{-6}	2.3 10^{-5}	23%

Table 1: Data related to collected droplets on the RDC surface obtained with $\dot{m}_0 = 110^{-4} kg/s$ for different droplet injection configurations: GIC, HIC, MIC and BIC.

Figure Captions

Figure 1. View of the investigated cabinet

Figure 2: Flow chart computational procedure used in the UDF to compute the deposited and evaporative flux of droplets on the RDC surface.

Figure 3. Schematization of boundary conditions used for numerical model

Figure 4. View of the mesh inside the cabinet

Figure 5. Evolution of radiative incident flux along the cabinet: Experimental values

Figure 6. Velocity field into the air curtain: a) Experimental results b) Numerical results.

Figure 7. Vertical profiles of the longitudinal *U* velocity (a) 0.05 (b) 0.3 m (c) 0.06 and (d) 0.75m.

Figure 8. Comparison between experimental and numerical results concerning the evolution of product surface temperatures along the cabinet.

Figure 9. Evolution of the net radiative exchange on the exposed surface of RDC: experimental and numerical data.

Figure 10. Influence of mist cooling on the surface temperature along the cabinet: Numerical and experimental results

Figure 11. Evolution of droplet deposition rate obtained numerically along the cabinet with an GIC configuration for different droplet mass flow rates: $\dot{m}_0 = 1\,10^{-04}$, $5\,10^{-05}$ and $3\,10^{-05}\,kg/s$

Figure 12. Numerical contours of droplet concentration within the air curtain obtained for global droplet injection configuration with $\dot{m}_0 = 1\,10^{-04}\,kg/s$.

Figure 13. Evolution of the droplet deposition rate along the cabinet with $\dot{m}_0 = 1\,10^{-04}\,kg/s$ for different droplet injection configurations: BIC (a), MIC (b), HIC (d), GIC (d).

Figure 14. Numerical contours of droplet concentration within the air curtain with $\dot{m}_0 = 1\,10^{-04}\,kg/s$ obtained for different droplet injection configurations: BIC, MIC, HIC and GIC.

Figure 15. Evolution of the surface temperature along the cabinet using GIC obtained numerically with the UDF: (a) GIC with $\dot{m}_0 = 2.2\,10^{-05}\,kg/s$, (b) MIC with $\dot{m}_0 = 1\,10^{-04}\,kg/s$ and $\dot{m}_0 = 2.6\,10^{-04}\,kg/s$

Figure 17. Experimental measurements of the surface temperature decrease in the downstream part of the cabinet obtained with mist flow in MIC for two droplet flow rate: $\dot{m}_0 = 1.1\,10^{-04}\,kg/s$ and $\dot{m}_0 = 1.7\,10^{-04}\,kg/s$.

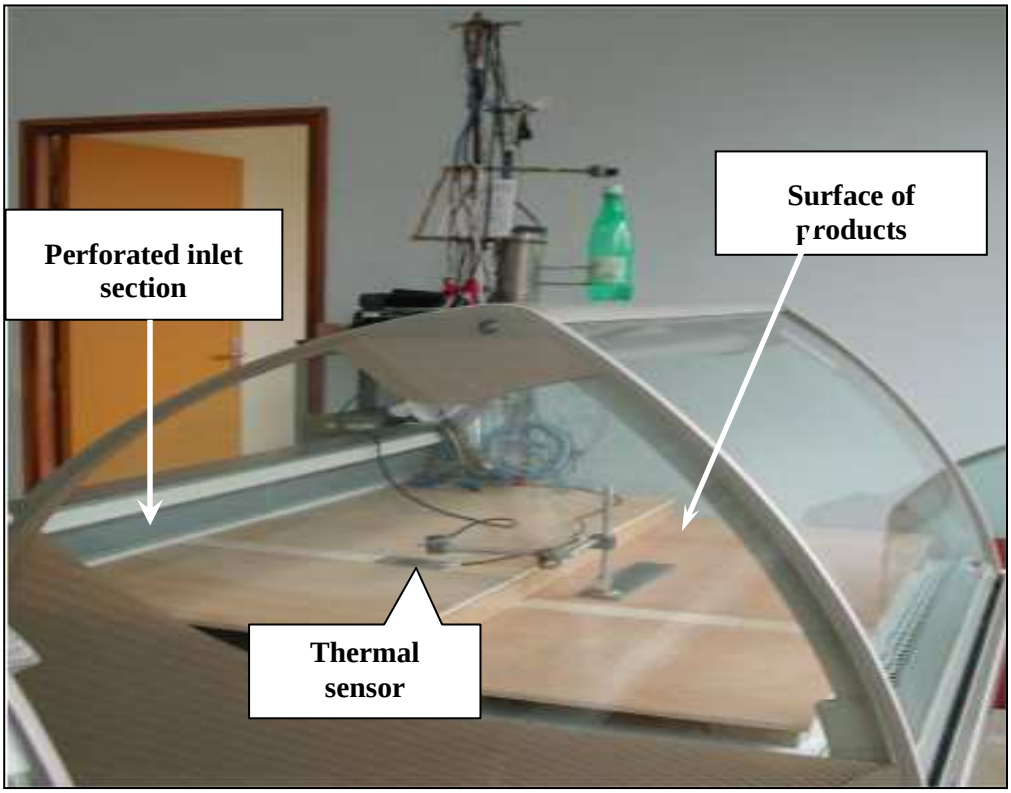
Perforated inlet section
Surface of products
Thermal sensor

Figure 1

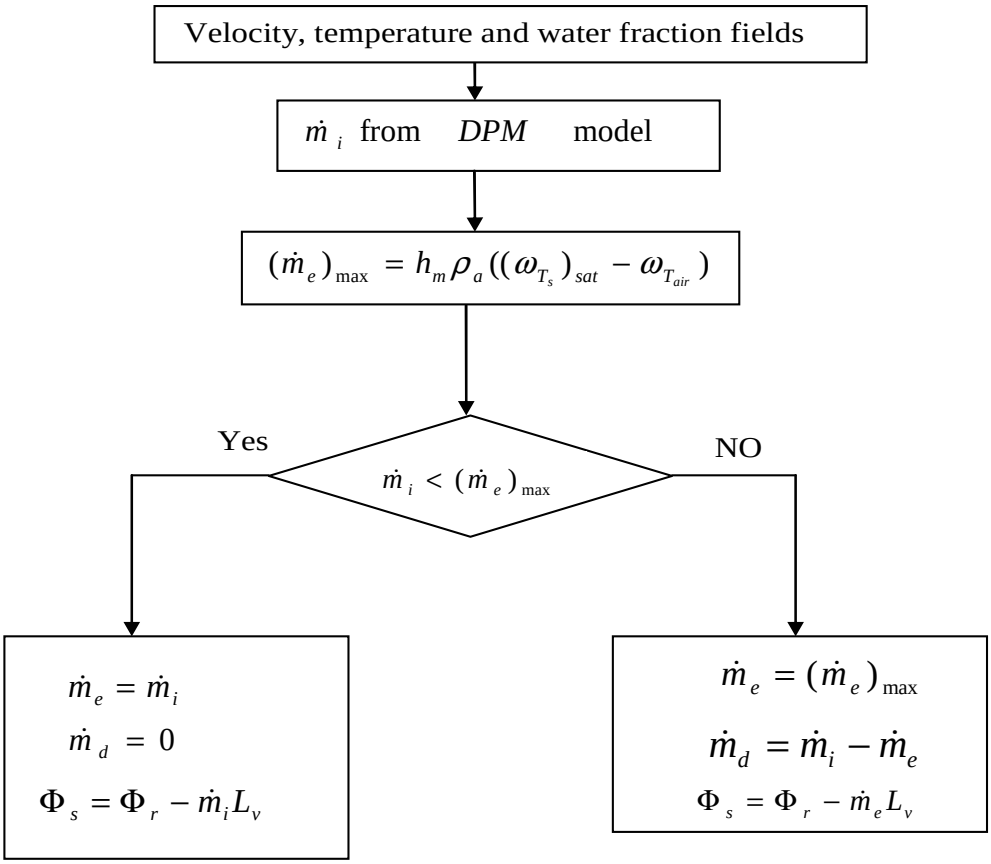
Velocity, temperature and water fraction fields
$\dot{m}_i$ from DPM model
$(\dot{m}_e)_{\max} = h_m \rho_a ((\omega_{T_s})_{sat} - \omega_{T_{air}})$
Yes
NO
$\dot{m}_i < (\dot{m}_e)_{\max}$
$\dot{m}_e = \dot{m}_i$
$\dot{m}_d = 0$
$\Phi_s = \Phi_r - \dot{m}_i L_v$
$\dot{m}_e = (\dot{m}_e)_{\max}$
$\dot{m}_d = \dot{m}_i - \dot{m}_e$
$\Phi_s = \Phi_r - \dot{m}_e L_v$

Figure 2

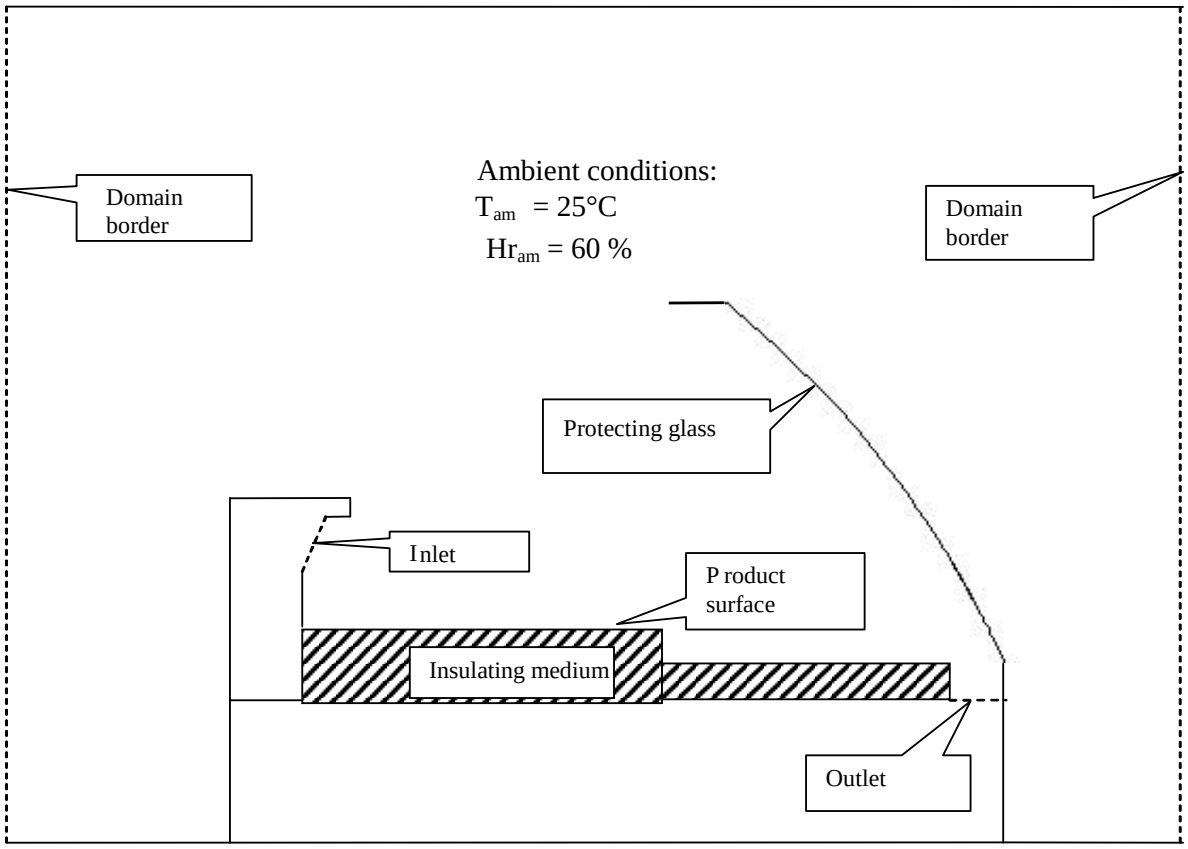
Domain
border
Ambient conditions:
T_{am} = 25°C
Hr_{am} = 60 %
Domain
border
Protecting glass
Inlet
P roduct
surface
Insulating medium
Outlet
Figure 3

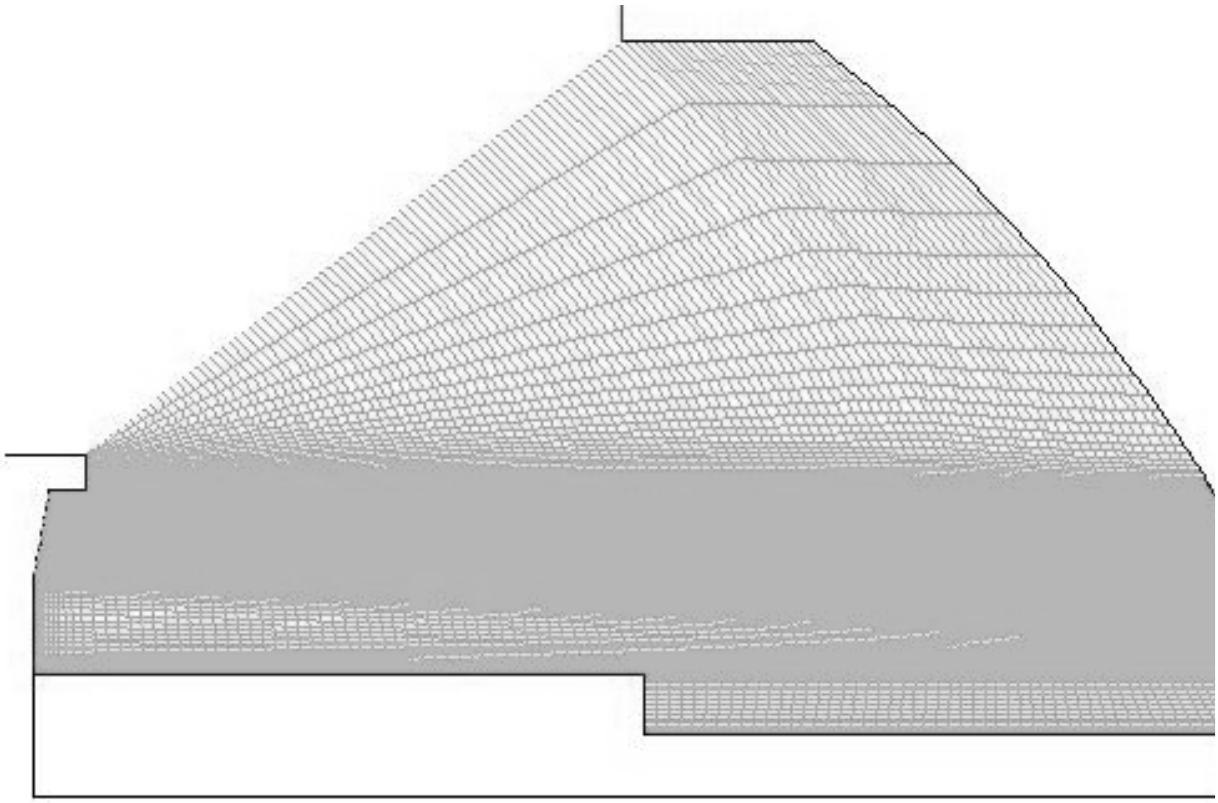

Figure 4

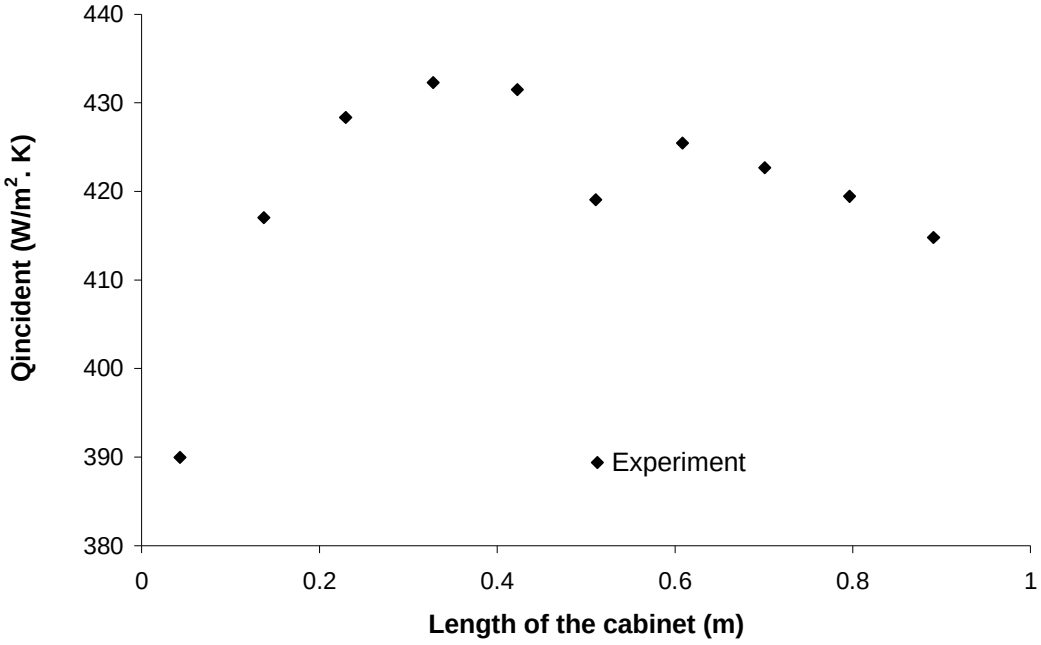
440
430
420
410
400
390
380
Qincident (W/m2. K)
0
0.2
0.4
0.6
0.8
1
Length of the cabinet (m)
Experiment

Figure 5

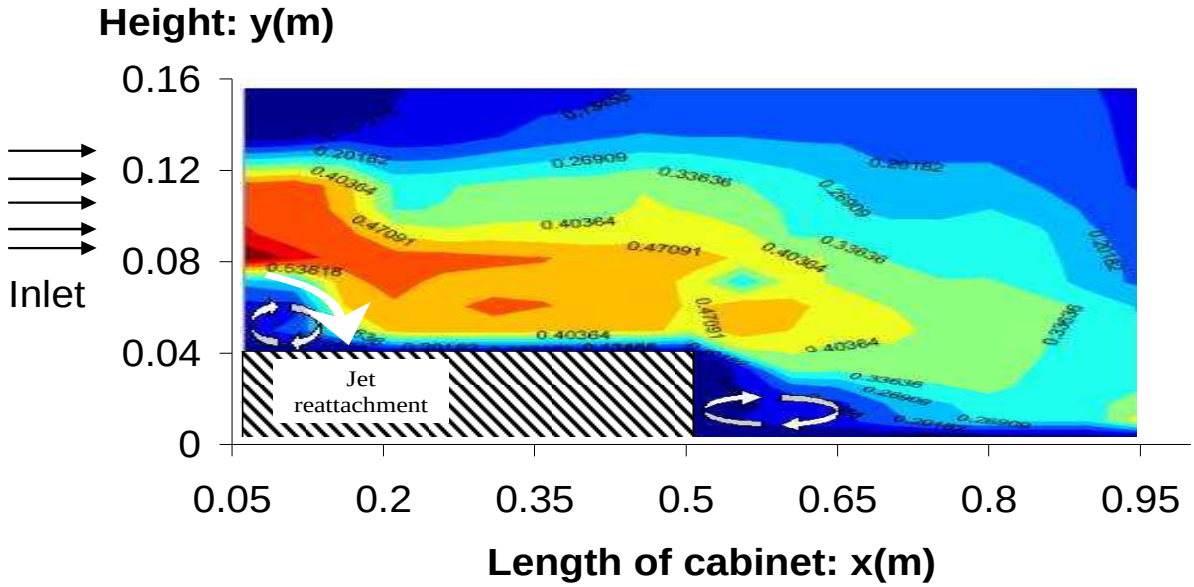
Height: y(m)
0.16
0.12
0.08
0.04
0
Inlet
Jet
reattachment
0.05
0.2
0.35
0.5
0.65
0.8
0.95
Length of cabinet: x(m)

a)

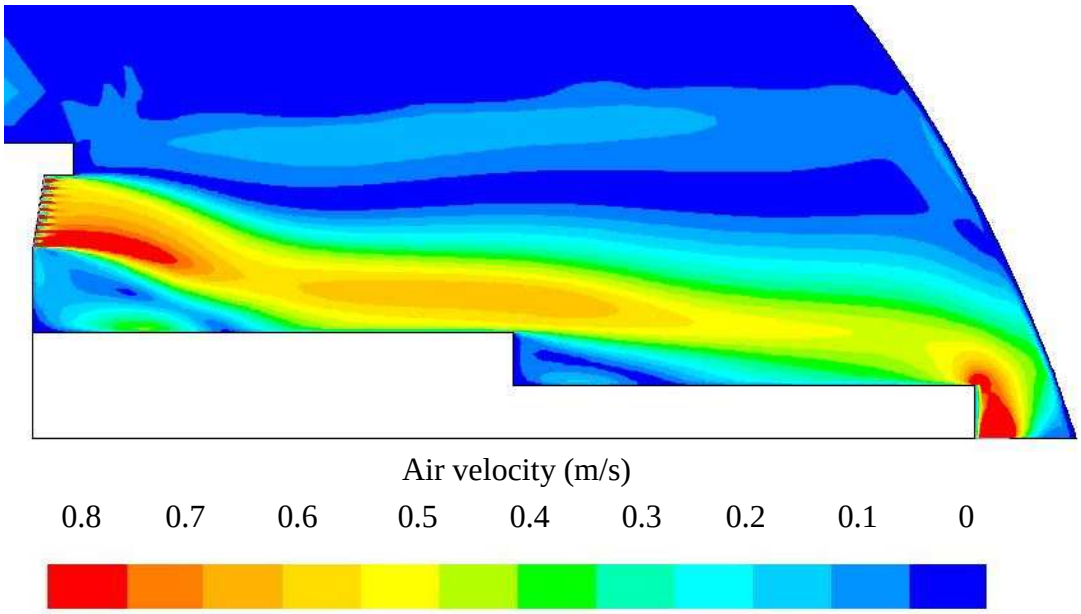
Air velocity (m/s)
0.8
0.7
0.6
0.5
0.4
0.3
0.2
0.1
0

b)

Figure 6

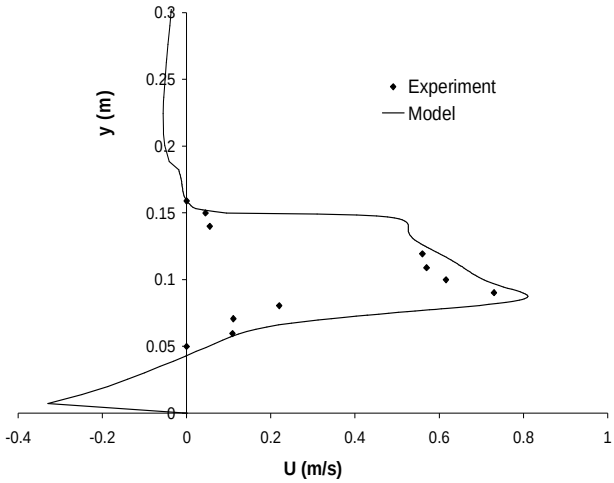

a) x=0.05 m

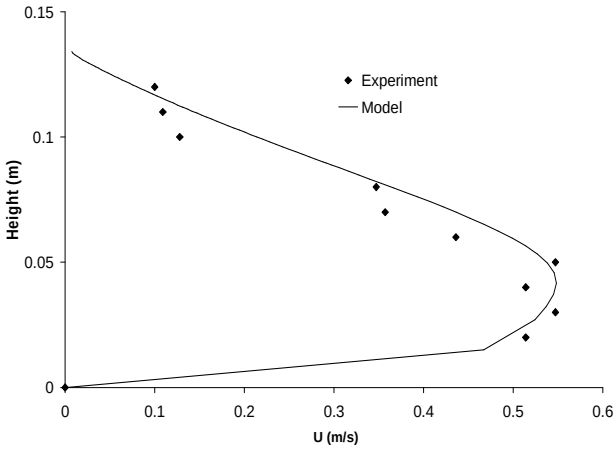

b) x=0.3 m

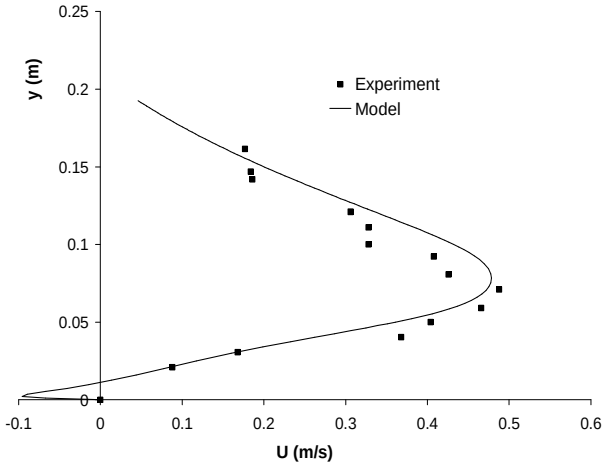

c) x=0.6 m

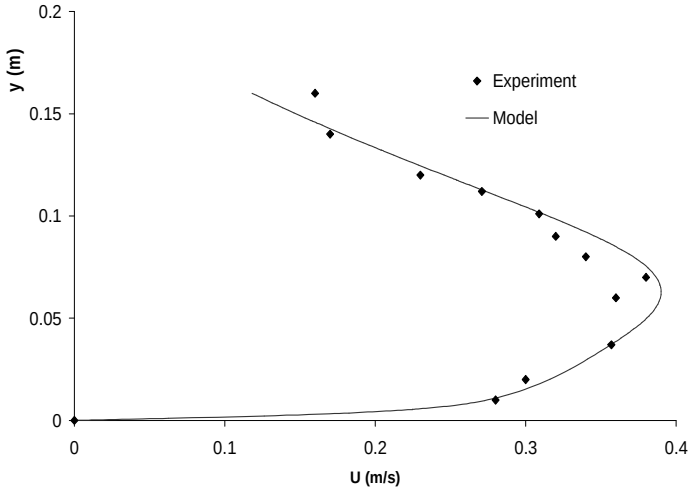

d) x= 0.75 m

Figure 7

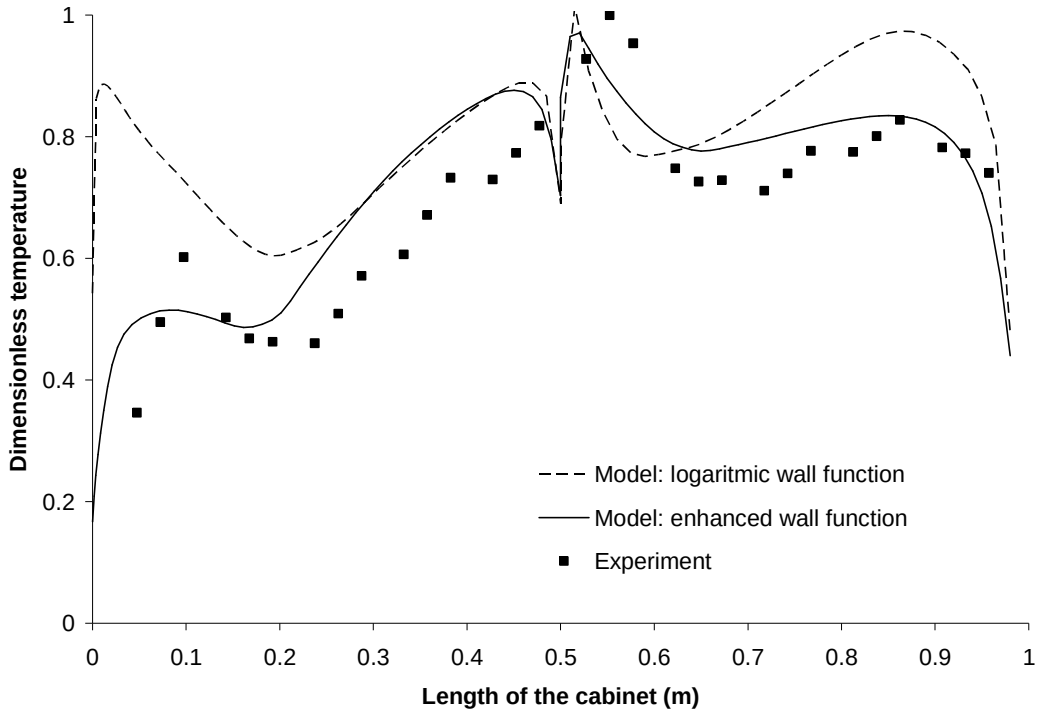
Dimensionless temperature
Length of the cabinet (m)
Model: logaritmic wall function
Model: enhanced wall function
Experiment
0
0.2
0.4
0.6
0.8
1
0.1
0.3
0.5
0.7
0.9

Figure 8

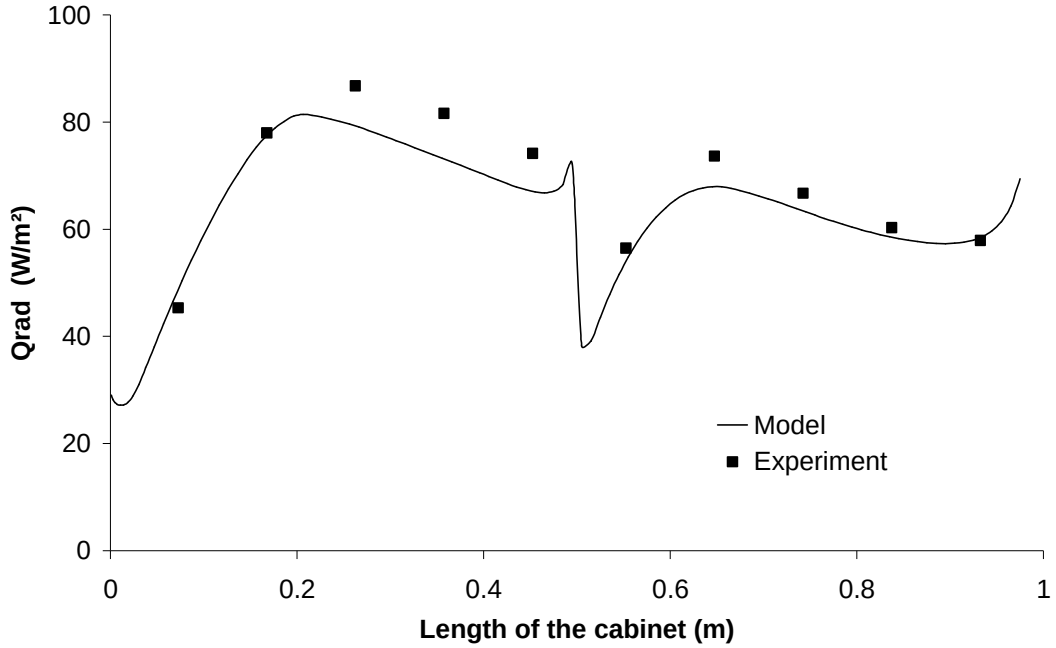
100
80
60
40
20
0
Qrad (W/m²)
0
0.2
0.4
0.6
0.8
1
Length of the cabinet (m)
Model
Experiment

Figure 9

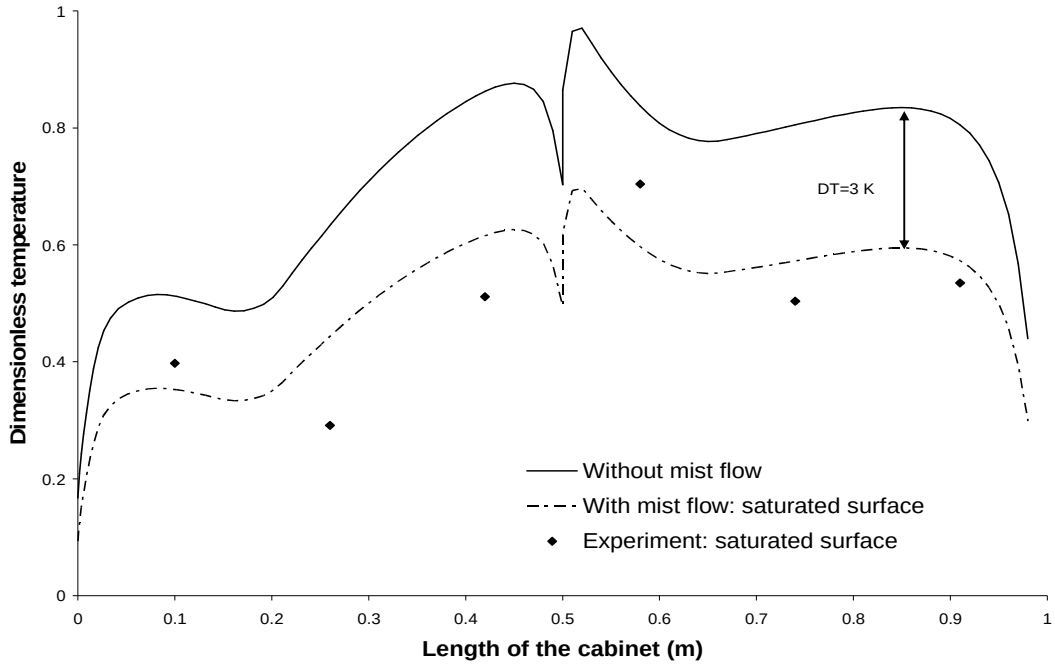
Dimensionless temperature
Length of the cabinet (m)
DT=3 K
Without mist flow
With mist flow: saturated surface
Experiment: saturated surface
0
0.2
0.4
0.6
0.8
1
0.1
0.2
0.3
0.4
0.5
0.6
0.7
0.8
0.9

Figure 10

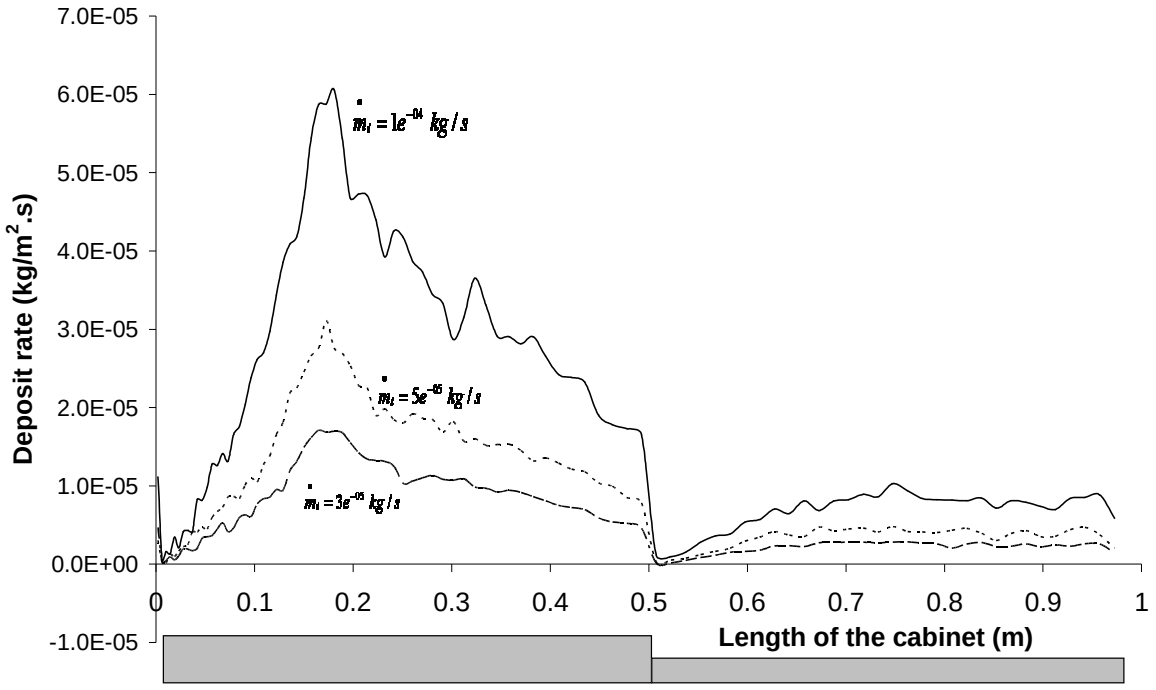
7.0E-05
6.0E-05
5.0E-05
4.0E-05
3.0E-05
2.0E-05
1.0E-05
0.0E+00
-1.0E-05
Deposit rate (kg/m2.s)
$\dot{m}_t = 1e^{-04}\ kg/s$
$\dot{m}_t = 5e^{-05}\ kg/s$
$\dot{m}_t = 3e^{-05}\ kg/s$
0
0.1
0.2
0.3
0.4
0.5
0.6
0.7
0.8
0.9
1
Length of the cabinet (m)

Figure 11

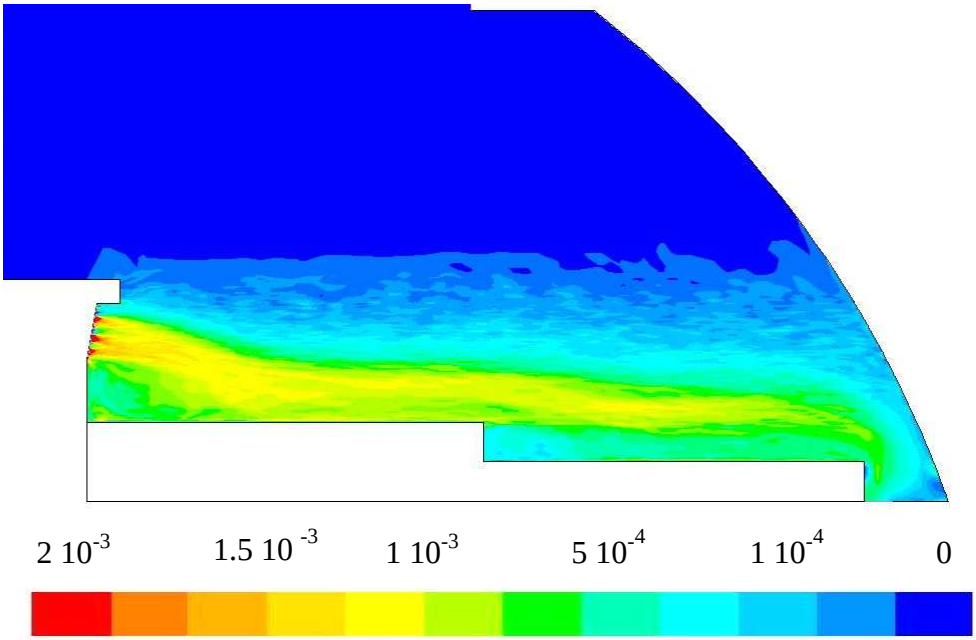

Figure 12

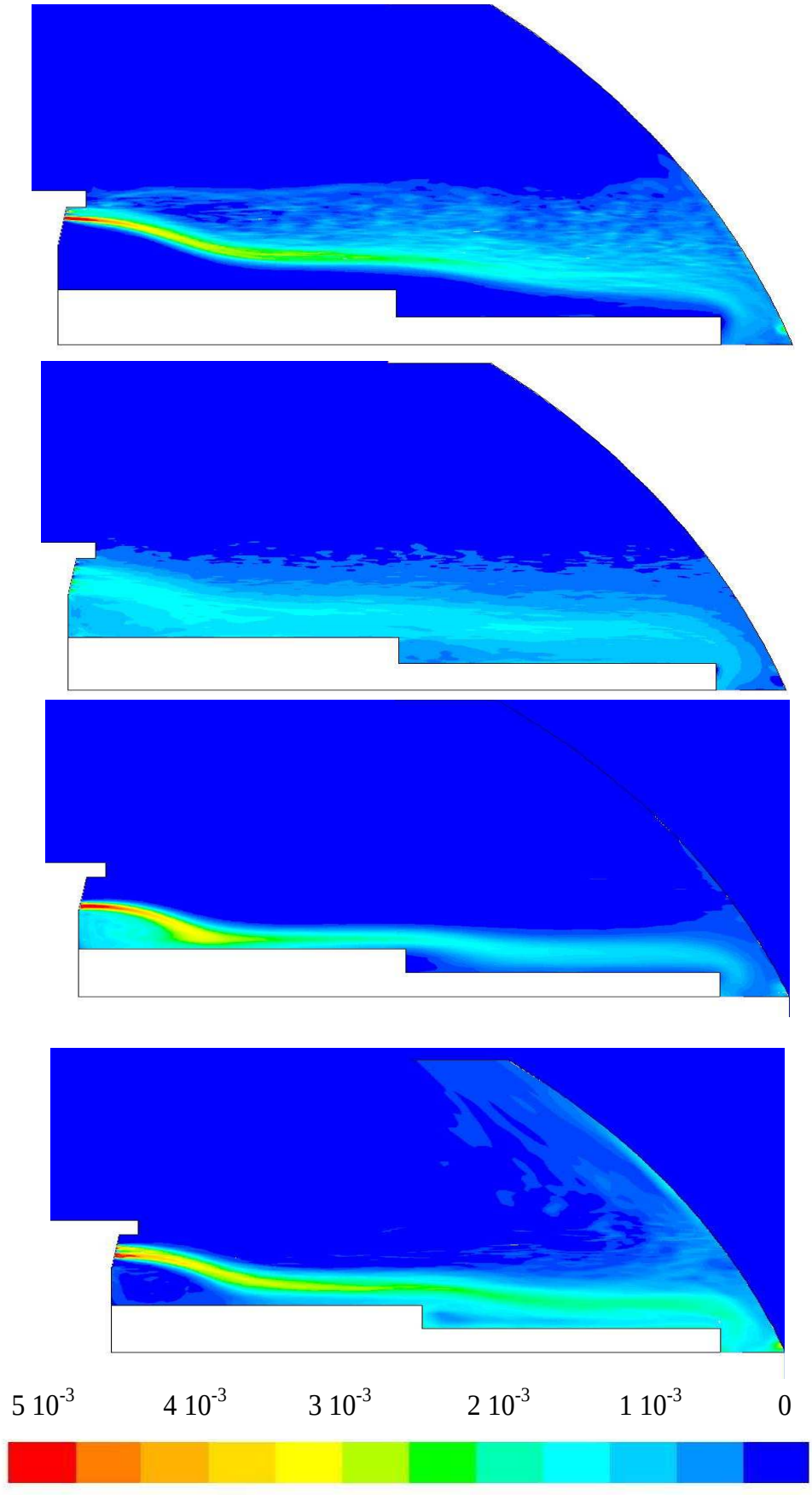

Figure 13

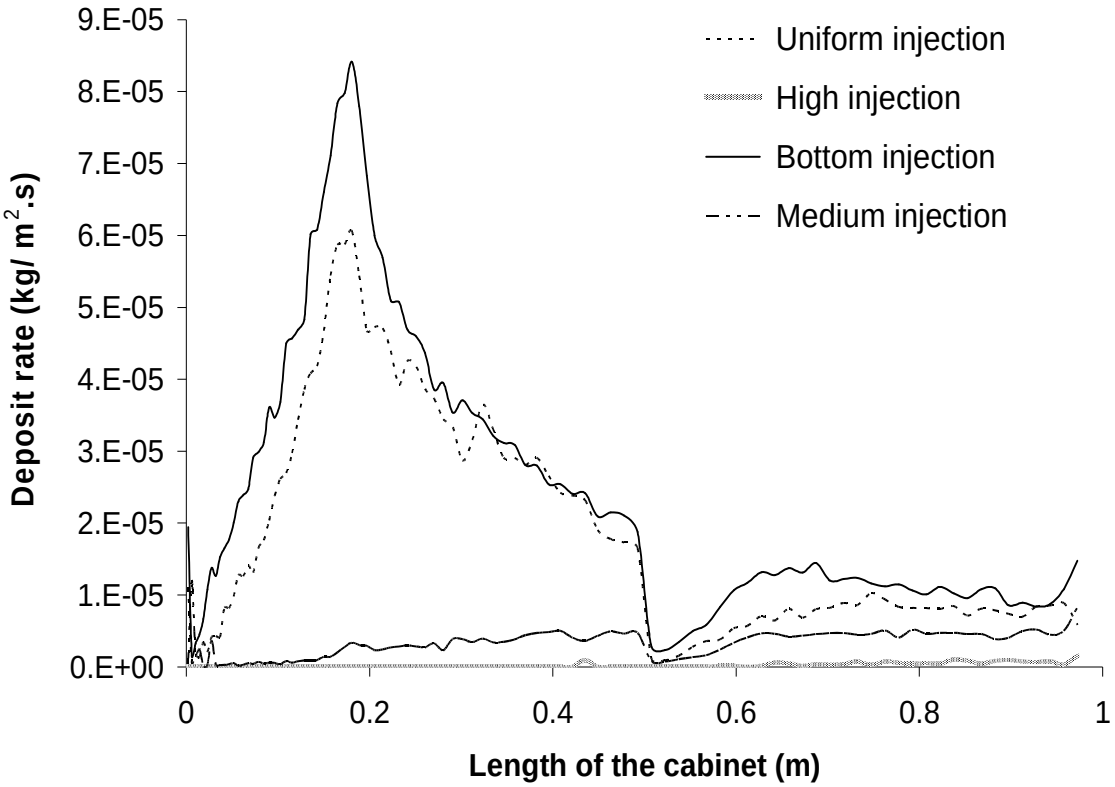
9.E-05
8.E-05
7.E-05
6.E-05
5.E-05
4.E-05
3.E-05
2.E-05
1.E-05
0.E+00
Deposit rate (kg/ m2.s)
0
0.2
0.4
0.6
0.8
1
Length of the cabinet (m)
Uniform injection
High injection
Bottom injection
Medium injection

Figure 14

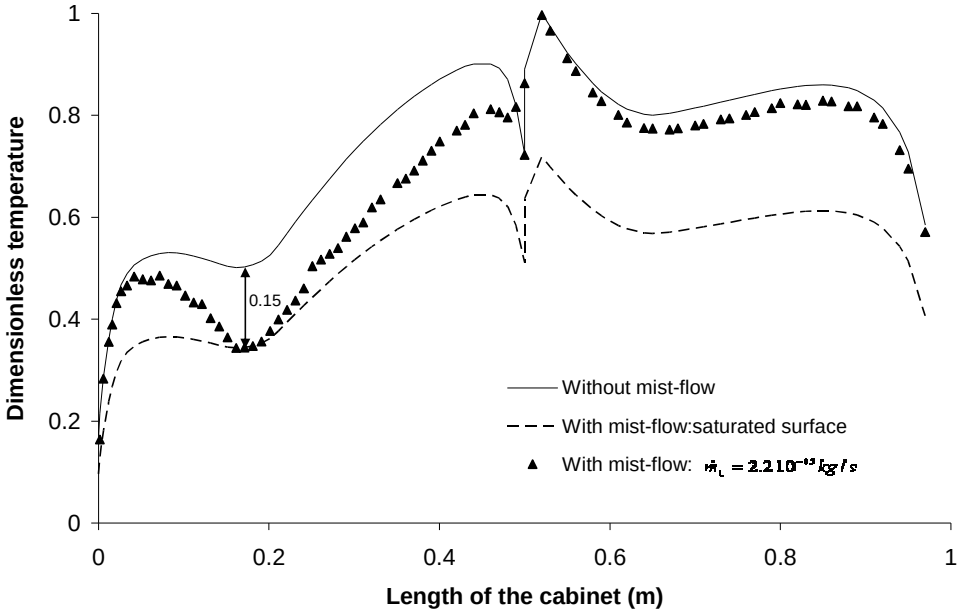
Dimensionless temperature
Length of the cabinet (m)
0.15
Without mist-flow
With mist-flow:saturated surface
With mist-flow: $\dot{m}_L = 2.2\,10^{-03}\,kg/s$

a)

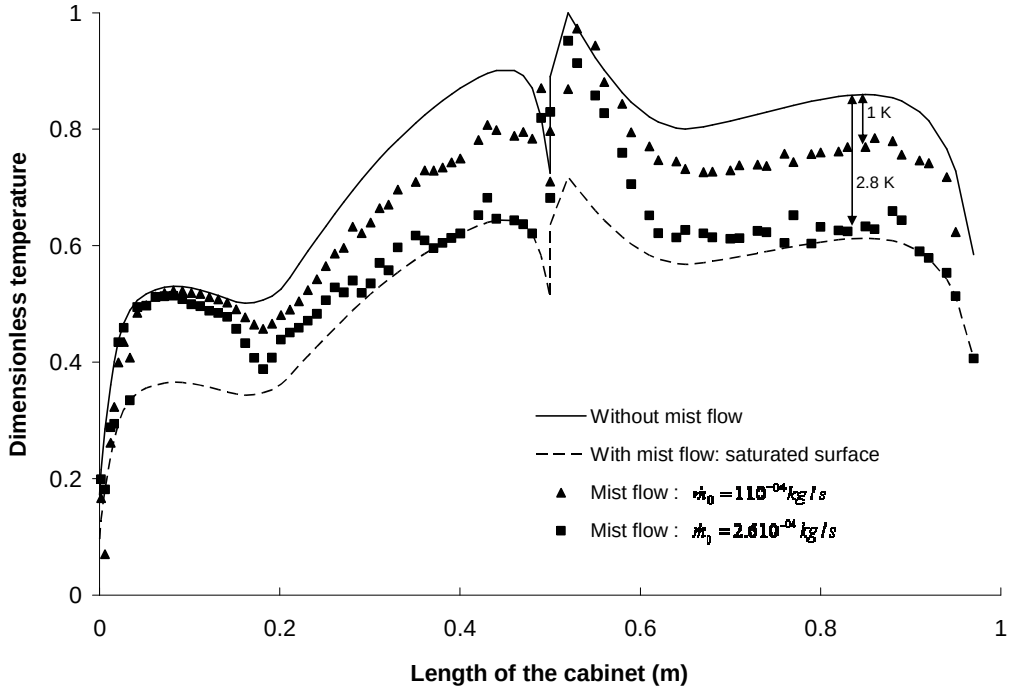
Dimensionless temperature
Length of the cabinet (m)
1 K
2.8 K
Without mist flow
With mist flow: saturated surface
Mist flow : $\dot{m}_0 = 1\,10^{-04}\,kg/s$
Mist flow : $\dot{m}_0 = 2.6\,10^{-04}\,kg/s$

b)

Figure 15

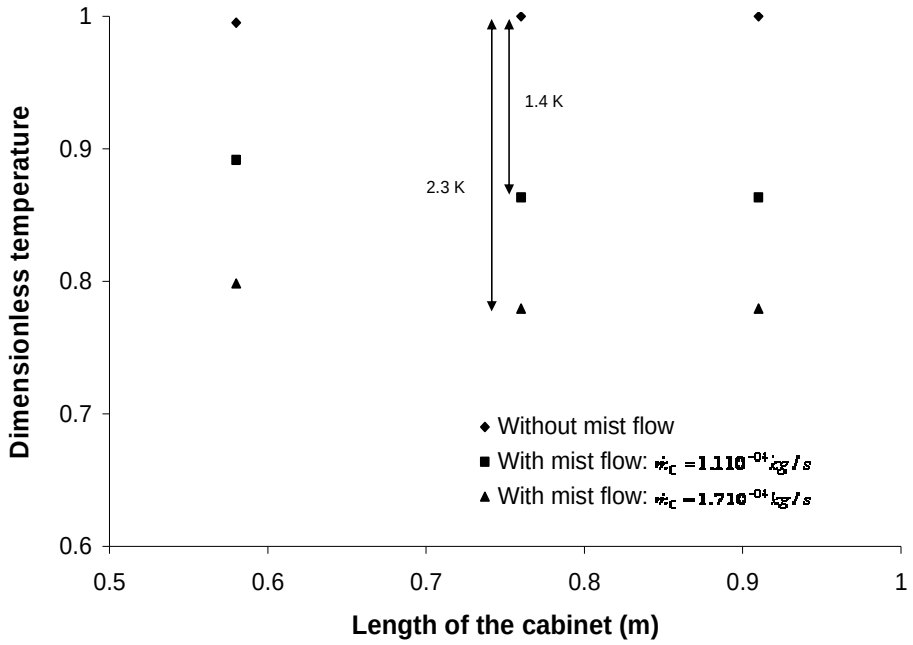
1
0.9
0.8
0.7
0.6
0.5
0.6
0.7
0.8
0.9
1
Dimensionless temperature
Length of the cabinet (m)
1.4 K
2.3 K
Without mist flow
With mist flow: $\dot{m}_c = 1.110^{-04} kg/s$
With mist flow: $\dot{m}_c = 1.710^{-04} kg/s$

Figure 16